Journal of Intelligent Manufacturing
https://doi.org/10.1007/s10845-023-02092-6

Monitoring and control of biological additive manufacturing using machine learning

Samuel Gerdes[1] · Aniruddha Gaikwad[1] · Srikanthan Ramesh[4] · Iris V. Rivero[2] · Ali Tamayol[3] · Prahalada Rao[1,5]

Received: 22 June 2022 / Accepted: 7 February 2023

Abstract

The goal of this work is the flaw-free, industrial-scale production of biological additive manufacturing of tissue constructs (Bio-AM). In pursuit of this goal, the objectives of this work in the context of extrusion-based Bio-AM of bone tissue constructs are twofold: (1) detect flaw formation using data from in-situ infrared thermocouple sensors; and (2) prevent flaw formation through preemptive process control. In realizing the first objective, data signatures acquired from in-situ sensors were analyzed using several machine learning approaches to ascertain critical quality metrics, such as print regime, strand width, strand height, and strand fusion severity. These quality metrics are intended to capture the process state at the basic 1D strand-level to the 2D layer-level. For this purpose, machine learning models were trained to classify and predict flaw formation. These models predicted print quality features with accuracy nearing 90%. In connection with the second objective, the previously trained machine learning models were used to preempt flaw formation by changing the process parameters (print velocity) during deposition—a form of feedforward control. With the feedforward process control, strand width heterogeneity was statistically significantly reduced, reducing the strand width difference between strand halves to less than 50 μm. Using this integrated process monitoring, detection, and control approach, we demonstrate consistent, repeatable production of Bio-AM constructs.

Keywords 3D printing · Bone tissue · Poly(caprolactone) (PCL)-hydroxyapatite (HAp) composites · In-situ sensing

Introduction

Background

An essential clinical practice for treating damaged, diseased, or lost tissues is through biological grafts (Samandari et al., 2021). These grafts fall under two classes: (1) grafts from elsewhere in the patient's own body (autograft), and (2) grafts from a donor to the patient (allograft) (Mostafavi et al., 2021a). Autografts are limited in availability and can treat tissues such as skin, tendon, muscle, and bone. Further, autografts can cause donor-site morbidity (Murphy & O'Brien, 2010). Comparatively, allografts have a broader scope, including whole organ transplants. However, allografts are still scarce, prone to rejection by a patient's immune system, and can transmit diseases (Murphy & O'Brien, 2010). A new area of research focusing on the direct production of tissues and organs for transplantation, known as tissue engineering, has been developed in response to these issues.

One emerging platform for tissue engineering, biological additive manufacturing (Bio-AM), has garnered attention to fabricate complex and biomimetic architectures. Bio-AM comprises five main production techniques: stereolithography, inkjet, laser-assisted, melt electro-writing, and extrusion-based printing (Heinrich et al., 2019; Samuel Gerdes et al., 2021). These print modalities are described

✉ Samuel Gerdes
samuel.e.gerdes@gmail.com

1 Mechanical and Materials Engineering, University of Nebraska-Lincoln, Lincoln, NE, USA

2 Industrial and Systems Engineering, Rochester Institute of Technology, Rochester, NY, USA

3 Biomedical Engineering, University of Connecticut, Farmington, CT, USA

4 School of Industrial Engineering and Management, Oklahoma State University, Stillwater, OK, USA

5 Grado Department of Industrial and Systems Engineering, Virginia Tech, Blacksburg, VA, USA

Published online: 06 March 2023

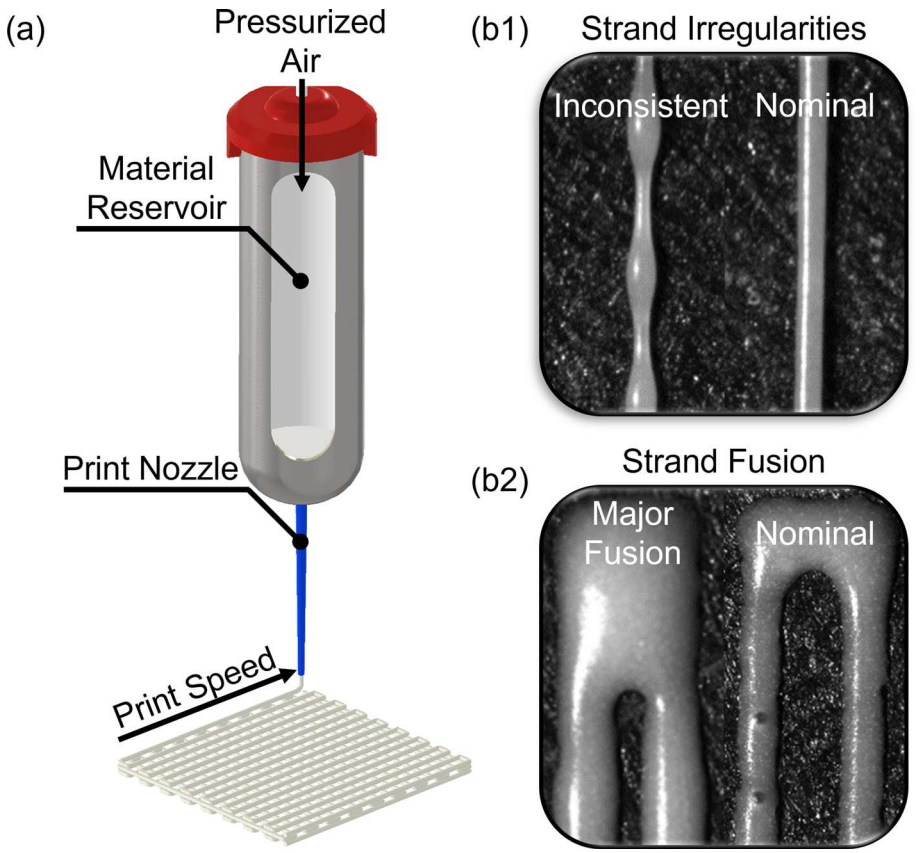

Fig. 1 Overview of the extrusion-based biological additive manufacturing process. **a** Schematic of the material deposition method in pneumatic extrusion-based biological additive manufacturing. **b1**, **b2** Demonstrations of two defect types in the extrusion-based process, strand quality and strand fusion defects

and explored in depth in the Bio-AM literature, detailing their inherent benefits and drawbacks (Heinrich et al., 2019; Ramesh et al., 2021). Of these print modalities, extrusion-based printing (Fig. 1a) is the most widely adopted form of Bio-AM due to its compatibility with an extensive range of material viscosities and its simplicity compared to other printing modalities (Derakhshanfar et al., 2018; Heinrich et al., 2019; Hölzl et al., 2016; Ribeiro et al., 2017). While extrusion-based (bio)printing allows the rapid fabrication of scaffolds with clinically relevant dimensions, it suffers from limited resolution and print defects. Therefore, in this study, we focus on the extrusion-based Bio-AM. We note that pneumatic extrusion is one of the widely used embodiments of extrusion Bio-AM, the other two being screw- and piston-based.

The clinical translation of extrusion-printed Bio-AM necessitates a defect-free, predictable, reproducible fabrication process. Several defect types have been discussed in the literature: undesirable strand diameter, non-homogeneous strands, strand fusion, and strand collapse (Habib et al., 2018; Habib & Khoda, 2019; Sam Gerdes et al., 2020; Samuel Gerdes et al., 2021; Soltan et al., 2019; Webb & Doyle, 2017). As these defects pertain typically to a single layer, it is imperative to reduce their occurrence. Otherwise, errors will propagate throughout the scaffold, leading to other defects (Sam Gerdes et al., 2020). This work focuses explicitly on undesirable strand width, non-homogenous strands, and strand fusion flaws created during the extrusion-based Bio-AM process, as exemplified in Fig. 1b1, b2. Additionally, strand fusion defects and collapse may also result from interactions between adjoining layers.

Undesirable strand width (Fig. 1b1), as the name entails, concerns disparity between the design and realized strands due to an improper coupling of the material flow rate and the print speed (Sam Gerdes et al., 2020). Print speed is inversely proportional to the localized deposition, the volume of material deposited at a given position for a set flow rate. As a result, low print speeds yield overly large strands (over-extrusion), and high print speeds yield small strands (under-extrusion if strands have discontinuity or a beaded appearance). Within the under-extrusion regime, non-homogeneous strands may be formed, as a uniform flow between the print tip and substrate cannot be maintained. Instead, periodic material deposition occurs when enough material collects at the tip and touches the substrate, creating sinusoidal-like strands.

Strand fusion (Fig. 1b2) pertains to coalescing adjacent strands, often propagating at turnaround sections through capillary forces or material spread due to gravity (Ribeiro et al., 2017). Strand fusion is inversely proportional to the distance between adjacent strands. As a result, over-extrusion

can increase the chance of strand fusion. We note that distance between adjacent strands is one of many factors which impact strand fusion, and it is important to consider the complex interaction of interstrand distance with needle diameter, substrate temperatures and deposition speed.

Print defects (flaws) not only affect the geometrical accuracy of a scaffold but also have the potential to alter the mechanical performance (Sam Gerdes et al., 2020), as well as the biological response (Samuel Gerdes et al., 2021). Intuitively, changes in scaffold geometry alter the cross-sectional areas for applied loads, which can alter the mechanical properties of the scaffold, such as the compressive modulus (Sam Gerdes et al., 2020). Further, flaws can alter the intentional pore spaces, impacting the biological response. For example, pore size in musculoskeletal tissue engineering and its effects on cellular response are documented for pores ranging from 20 to 1500 μm (Haglund et al., 2019; Hulbert et al., 1970; Jenkins & Little, 2019; Lee et al., 2004; Mostafavi et al., 2021b; Nehrer et al., 1997; Williams et al., 2005). Specifically, small pores (75–135 μm) have increased cell adhesion and osteochondral differentiation, while large pores (> 300 μm) are required for vascularization and bone ingrowth (Chen et al., 2020; Hulbert et al., 1970; Jenkins & Little, 2019; Klawitter et al., 1976; Kuboki et al., 2001; Murphy & O'Brien, 2010; Roosa et al., 2010; Tsuruga et al., 1997). Because of the risk print defects pose to the functionality of printed tissue engineering scaffolds, it is vital to negate defect occurrence.

Objective, prior work, and novelty

In response to the need for tissue engineering scaffolds, the goal of this work is to ensure the flaw-free production of scaffolds in extrusion-based Bio-AM. Towards this goal, one objective of this work is to detect flaw formation in Bio-AM constructs as they develop, using data acquired from in-situ sensors. To that end, this work implements IR thermocouple-based sensing to gather in-situ data about the printing process. Machine learning approaches were subsequently implemented to analyze the sensor data and ultimately predict strand quality and the severity of strand fusion.

The second objective toward the goal of flaw-free production is to prevent defects before they occur in the scaffold. Towards this objective, preemptive process control was deployed to determine aspects of part quality prior to printing and find corrective print parameter changes to improve print homogeneity. While the aim to control defect occurrence in extrusion-based Bio-AM is not novel, this method is a significantly different approach than those presented in the current literature, detailed in the remainder of this section.

Two distinct pathways have developed in the literature to overcome defect occurrence in extrusion-based printing: process optimization and process monitoring. In the former, the goal is to improve the understanding of causal process parameter-flaw relationships, ultimately leading to an optimized print parameter arrangement for a material and processing condition (Armstrong et al., 2021). In the latter, an effort is taken to capture the essential features indicative of the print quality in real-time, allowing for the alteration or cessation of the printing process in response.

Process optimization has been applied to the primary defect types such as undesirable strand diameter, strand non-homogeneity, strand fusion, strand collapse, and pore geometry variability, and descriptions of the various optimization strategies for different defects are presented in our prior work (Samuel Gerdes et al., 2021). One example is the mitigation of undesirable strand width. To optimize the strand width, print parameter tests are conducted across possible print speeds or pressures, and the resulting strand width is observed (Cheng et al., 2017; Habib et al., 2018; Habib & Khoda, 2019; He et al., 2016; Sam Gerdes et al., 2020; Soltan et al., 2019; Thattaruparambil Raveendran et al., 2019; Webb & Doyle, 2017; Zehnder et al., 2015).

While process optimization can improve print quality, this build-and-test approach has significant limitations (Cheng et al., 2017; Habib et al., 2018; Habib & Khoda, 2019; He et al., 2016; Sam Gerdes et al., 2020; Soltan et al., 2019; Thattaruparambil Raveendran et al., 2019; Webb & Doyle, 2017; Zehnder et al., 2015). First, process optimization assumes that print parameters are prevailing influencers of part quality. Additional considerations such as the effect of rapid acceleration in the bed and nozzle motion or the contribution of the construct geometry to defect formation are neglected. Second, process optimization requires thorough testing of the print parameters and material compositions to achieve an optimal result. Due to this experimental burden, exhaustive process optimization testing is not compatible with the scope of all projects. While this burden could be eased by referring to the literature for a specific material, print parameters from one printer may not yield the same results on another printer.

Third, empirical process optimization is not scalable. In other words, optimizing strand width, strand fusion, strand collapse, and pore geometry are multi-scale challenges. As a result, an optimal parameter arrangement in one scale may not transfer to another. Moreover, process optimization does not offer a means of actual process control. Under traditional process optimization, measurements are conducted post-print, making it only possible to assess print quality after the print has concluded, potentially wasting time and resources (Cheng et al., 2017; Habib et al., 2018; Habib & Khoda, 2019; He et al., 2016; Sam Gerdes et al., 2020; Soltan et al., 2019; Thattaruparambil Raveendran et al., 2019; Webb & Doyle, 2017; Zehnder et al., 2015).

Due to the limitations of build-and-test process optimization, growing attention has been placed on process

monitoring to assess and control flaws during the printing process. One means of process monitoring is topology measurement after each layer is deposited (Armstrong et al., 2019, 2020, 2021; Yang et al., 2021). In recent work by Armstrong et al. (Armstrong et al., 2019, 2020, 2021), topology measurement was conducted with 3D laser scanning. Corrections were made to the print path and print parameters to reduce 2D errors in strand placement, width, and turnaround quality (Armstrong et al., 2019, 2020, 2021). However, the alterations in the print path and parameters had to be made iteratively; several print trials were conducted, and alterations were made between each print to lead to a more optimized print. While this process monitoring approach improves print quality, it has drawbacks. Primarily, the approach requires several trials to converge on acceptable print quality. Secondly, the converged solution is unique to the material composition, and design architecture, requiring more tuning should the design be changed later.

In contrast, Yang et al., 2021 have developed a monitoring system based on optical coherence tomography (OCT). In OCT, light is directed at the scaffold, reflecting light from the subsurface level, which is then collected, and the optical path length allows for 3D modeling of the scaffold. In contrast to laser scanning, which does not penetrate to the internal scaffold structure, OCT can acquire subsurface information. With OCT, Yang et al. demonstrated the characterization of layer thickness, strand width, and pore size (Yang et al., 2021).

In addition to topology-based defect detection, there is an emerging trend in applying machine learning for process monitoring in Bio-AM (Yu & Jiang, 2020). The use of machine learning in other additive manufacturing processes is documented extensively and can provide new avenues of advancement for extrusion-based Bio-AM (Yu & Jiang, 2020). For instance, the work of Scime & Beuth, 2019 in laser powder bed fusion showed the use of unsupervised machine learning on meltpool images to determine meltpool quality. In the work of Gaikwad et al., 2020, a hybrid in-situ sensing system for laser powder bed fusion was formed with a high-speed video camera and a pyrometer. With the use of in-situ sensing-derived features, Gaikwad et al., 2020 enabled the assessment of single strand quality with machine learning. In the recent work of Jin et al., 2021, similar monitoring principles were implemented in Bio-AM; layer-wise imaging was coupled with deep learning to classify three types of anomalies in patches of the layer image.

While still a new and developing research path, it is valuable to note that process monitoring in Bio-AM is currently limited to the layer level. With topology scanning and layer imaging, all process sensing is conducted after a layer is completed, neglecting the possibility of defect detection during a layer. As a result, there is a substantial deficit in the sensing of defects during layer printing through the monitoring of the extrusion and the most critical part of extrusion-based printing, strand formation. Therefore, this research aims to develop a monitoring system capable of capturing the quality of extrusion-based Bio-AM scaffolds as they are printed instead of after a layer (Fig. 2). In addition, this research presents a preliminary means of feedforward process control featuring the adaptation of print speed to combat print defect occurrence (Fig. 2).

This paper is organized in the following manner. Sect. "Methodology" details the experimental methodology of the print materials and sensing setup (Sect. "Experimental setup"), specific experiments at strand and layer levels (Sect. "Experimental design"), in-situ measurement procedures for each experiment (Sect. "Feature extraction from in-situ sensor data"), and the basis for machine learning for predicting print quality from sensor data (Sect. "Quality prediction using machine learning"). In Sect. "Results", the effects of process parameters on strand and fusion quality, followed by the results of applying machine learning to predict print quality targets. Sect. "Results" also dives into feedforward process control of strand homogeneity in Sect. "Preemptive process control". Finally, Sect. "Conclusions and future work" summarizes the main conclusions from this work.

Methodology

Experimental setup

All experiments were conducted on an Allevi 3 extrusion-based 3D printer. The printer was supplemented with a heterogeneous sensor array to produce in-situ data during the printing process. As shown in Fig. 3, the in-situ sensing array consisted of two infrared (IR) thermocouples focused on the deposition pool (see Fig. 3a, b) and a layer optical imaging camera (see Fig. 3c). Layer imaging was conducted using a Blackfly S (BFS-U3-63S4M-C) camera with a telecentric lens (0.50X, 1/1.8" SilverTL) from Edmund Optics (NJ, USA). The IR thermocouples were selected based on our previous work in extrusion printing with non-biomaterials, where thermocouples were found to be adept at capturing nozzle clogs, deposition failures, and surface temperature (Rao et al., 2015; Roy et al., 2019).

The camera and lens produce an imaging region of approximately 14 mm × 10 mm, and the telecentric lens produces an image with a uniform scale throughout. The IR thermocouples (CSmicro LT22H) were purchased from Optris Infrared Sensing (NH, USA), with confocal lenses to focus the monitoring area further. The IR thermocouple sampling rate was set to 500 Hz for all experiments. Apart from the onboard sensing array, a 2D laser profiler (LJ-V7200) from Keyence (IL, USA) was used to measure the strand height post-print in single strand quality testing.

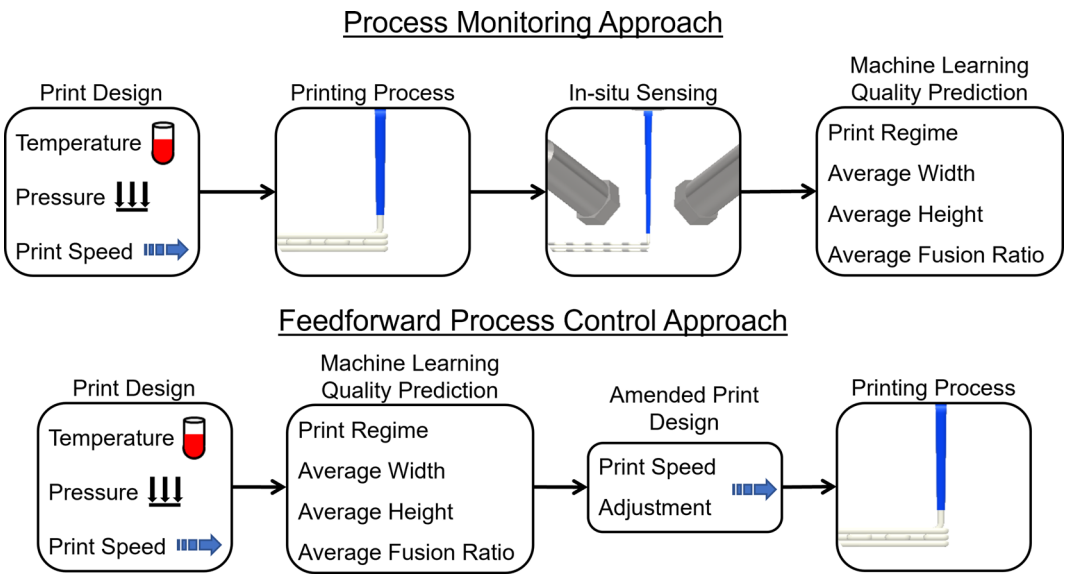

Fig. 2 Workflow schematics of both approaches presented in this work. (top row) In-situ sensing was coupled with machine learning for print quality prediction of the printing process. (bottom row) Feedforward process control to determine print speed amendments to reduce strand width heterogeneity

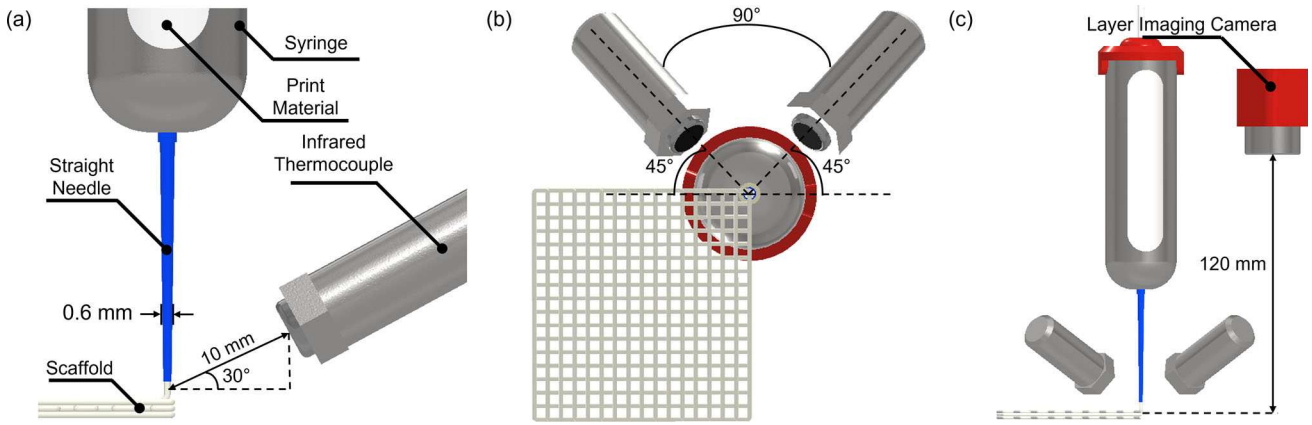

Fig. 3 Additive manufacturing of PCL/HAp using in-situ sensing of the geometrical outcome. **a** Side view of infrared thermocouple setup on the bioprinter. **b** Underside view of the infrared thermocouple placement. **c** Front view of the bioprinter outfitted with an in-situ monitoring system comprised of layer imaging and infrared thermal sensing

We note that several other process phenomena influence the print quality, such as bulk part temperature, heat flux, instantaneous viscosity, flow rate/behavior, local shear stress in the material, among others. However, these aspects are difficult, if not impossible, to measure in extrusion-based printing due to the limited access to sense these phenomena. This work takes the first critical step towards assessing the fidelity of the temperature and imaging measurements for enhanced process monitoring applications.

In closing this section, we note that, in this work, data from printing of the first layer is primarily used. Accordingly, there are potential concerns that the IR thermocouple data would be confounded by the temperature of the proceeding layers when used for a complex multi-layer part. However, since the IR sensors are focused over a narrow 0.6 mm diameter spot size (in line with our ideal strand width), producing a field-of-view of $-$ 0.28 mm^2 aimed near the extruder needle tip, the strands in the layer below would have a minimal effect.

Experimental design

Polycaprolactone (PCL, molecular weight = 14,000 Da)/hydroxyapatite (HAp, 2.5 μm powder) print materials were purchased from Sigma-Aldrich (MO, USA).

PCL and HAp were combined to form a 70/30 composition by weight (%PCL/%HAp w/w), and the composition underwent cryomilling to produce a more homogenous mixture and powder size. In our previous study, this PCL/HAp ratio proved compatible with human mesenchymal stem cells (hMSCs) and promoted bone development (material osteoconductivity) (Sam Gerdes et al., 2020). While the 80/20 and 70/30 PCL/HAp compositions showed comparable biological results (Sam Gerdes et al., 2020), the 70/30 composition provided a more challenging print material due to its increased viscosity. As a result, the printability issues must be addressed with quality assurance measures.

Experiments were divided into two phases: (1) single strand quality and (2) strand fusion assessment. Before printing, 70/30 PCL/HAp cryomilled powder was loaded into a stainless-steel syringe barrel and melted at a process condition-dependent temperature (130 or 140 °C) and held at temperature for 45 min prior to printing. The print material was pneumatically extruded through a 0.6 mm inner diameter stainless steel needle with straight walls (10 mm in length). For all experiments, set parameters for print bed temperature (20 °C), needle tip to substrate distance (0.4 mm), and pre- and post-flow durations (0 s for each) were used. Following layer completion, in-situ imaging of the layer was conducted.

Single strand quality

Extrusion-based printing is primarily governed by three interlinked process parameters: pressure, temperature, and print speed. For instance, pressure and temperature directly control material throughput, with temperature impacting material viscosity (resistance to flow) and pressure instigating material flow. Further, print speed governs the localized deposition of print material, as shown in Fig. 4.

If print speed is relatively higher than the material flow, under-extrusion occurs, and variable or discontinuous strands are observed (Fig. 4a, b). Balancing the print speed with the material flow produces ideal extrusion and homogenous strands analogous to the needle diameter (Fig. 4c). Finally, insufficient print speeds for the material flow yield over-extrusion, forming larger than desired strands (Fig. 4d). In summary, improper print parameter combinations lead to unfavorable strand quality, where strands significantly deviate from the intended design.

To assess print parameter effects on strand quality, experiments were conducted across twenty temperature–pressure-print speed combinations consisting of two temperatures (130 and 140 °C), two pressures (1.5 and 2.0 bar), and five print speeds (6, 8, 10, 12, and 14 mm/s). Six replicate 50 mm strands were formed and imaged at each processing condition. Upon completion of a strand, a dwell time of 25 s was used before printing the next strand to better distinguish between the sensing signatures.

The first 5 mm of each strand was omitted, because without initializing the flow prior to movement (pre-flow), this region will likely not achieve complete deposition along its length. Additionally, the final 5 mm of each strand was omitted to avoid considering the rounded strand end in width determination. While neglecting the starting and stopping regions prevents the ability to detect flaws pertaining to those regions, the infrared thermocouple system cannot instantaneously detect a temperature change, it takes around a second of printing before an elevated profile can be seen as the IR thermocouple starts collecting enough IR radiation to deviate from its previous baseline. This makes the starting points a similar reading to the substrate, and the end points congruent to the latter half of the line.

The remaining 40 mm in a strand was divided into four segments, each a 10 mm section of a strand, due to the limited field of view of the optical camera. Binarization was conducted, wherein the strand and background pixels were given 1 and 0 values, respectively. Image analysis was performed to measure strand continuity and width at the four imaged regions (Fig. 5). In practice, this start-and-stop error can be mitigated by printing a sacrificial sample, or through a pre-deposition pass.

In addition to strand width measurement, 2D laser profilometry was conducted at four points along each strand and averaged to estimate strand height for all the processing conditions. During strand height measurement, the four measured points were spaced to align with the midsection of each imaged region. Subsequently, the data was processed to classify the strand visually as follows: under-extrusion (discontinuous or having variable strand width), ideal extrusion (nominal strand quality), and over-extrusion (strands much larger than the 0.6 mm desired width).

Assessment of strand fusion

In addition to printing high-quality single strands, extrusion-based printing must accurately print along turns and corners. One frequent occurrence is right-angle printing, which can accumulate material in the inner corner due to the overlapping deposition area. Further, the PCL/HAp print material can spread and fuse before solidification, especially when two right-angle turns are made without sufficient distance between the turns. To observe the critical gap between turns, specialized artifacts were made with a gradient of gap spaces (Fig. 6a). Lines of 20 mm length were printed in these fusion test samples, followed by a turnaround with a specific inter-strand gap, and this sequence was repeated throughout the artifact. This strand fusion test artifact was motivated from prior work by other researchers in the literature (Habib & Khoda, 2019; Habib et al., 2018). A dwell time of 25 s was used upon completion of an artifact before printing the next artifact to better distinguish between the sensing signatures.

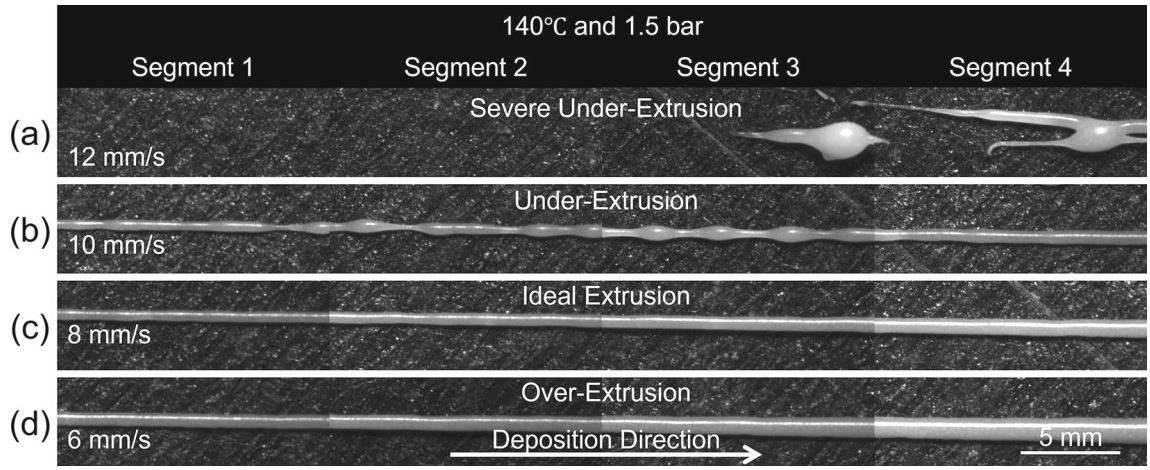

Fig. 4 Effect of print speed on single strand morphology. Three print regimes are formed by coupling extrusion temperature, pressure, and print speed. **a** Under-extrusion results from excessively high print speed for the established flow. **b** As print speed diminishes, under-extrusion reduces, and the critical strand breakdown point may be observed, where highly variable strand widths are formed. **c** Further reduction in print speed yields nominal or ideal extrusion, producing favorable strand width. **d** Inadequate print speed for the established flow yields over-extrusion, forming larger than desired strand widths

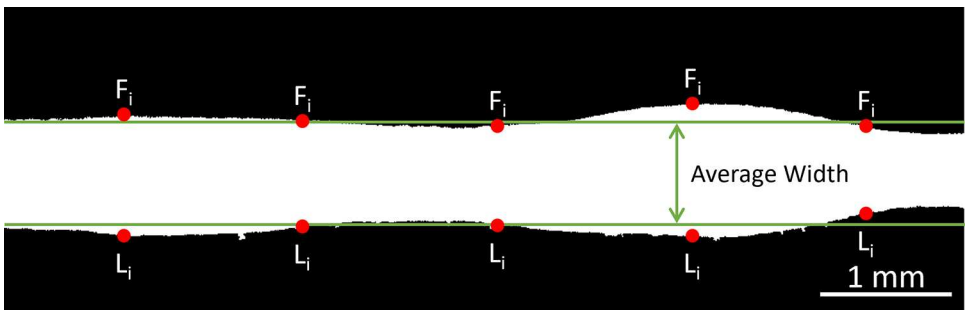

Fig. 5 Strand width assessment averaging the width between the first pixel index (F_i) and last pixel index (L_i) along the strand length for the segment's average strand width

Fusion test artifacts were created at two levels of temperature (130 and 140 °C) and two levels of pressure (1.5 and 2.0 bar) with print speeds that produced the three print regimes assessed in the single strand quality testing (over-extrusion, ideal extrusion, and under-extrusion). Each process condition (print regime) combination was printed across an interstrand gradient of 0.50, 0.75, 1.00, 1.25, 1.50, 1.75, 2.00, and 2.25 mm (Fig. 6a). Each interstrand gap was printed twice per artifact, and three artifacts were printed for six total replicates.

In Fig. 6b, images of artifacts deposited at constant temperature and pressure visually show the effect of print speed on strand fusion. Following printing, the artifact turnarounds were imaged and characterized. Once imaged, an average fusion length was constructed at each turnaround with a 100-point average starting at the turnaround center and progressing towards the turnaround's edge (see Fig. 7).

The rationale behind the 100-point average was that the imaging resolution was 204 pixels/mm, and a 100-point/pixel average amounts to a measurement region of 0.5 mm. If the fusion length were determined with a larger number of points, the measurement region for the 0.5 mm interstrand gaps would include a portion of the adjacent strands, leading to an incorrect average fusion length value. The turnarounds were assumed symmetric, such that the measurement region's direction from the turnaround center is inconsequential.

Fusion length was determined as the distance between the artifact's exterior edge to the opposite edge of the fusion region at a turnaround section. As shown in Fig. 7, the fusion lengths within the measurement region were the distances between the first pixel index (F_i) and last pixel index (L_i) of the largest interconnected region at a point. The fusion ratio (F_R) was then characterized as the ratio between the fusion length (F_L) and design width (W_D) of 0.6 mm. Importantly, using the design width in the fusion ratio calculation standardized the quality metric across the different interstrand spacings and fusion severities, providing a benchmark metric to compare results.

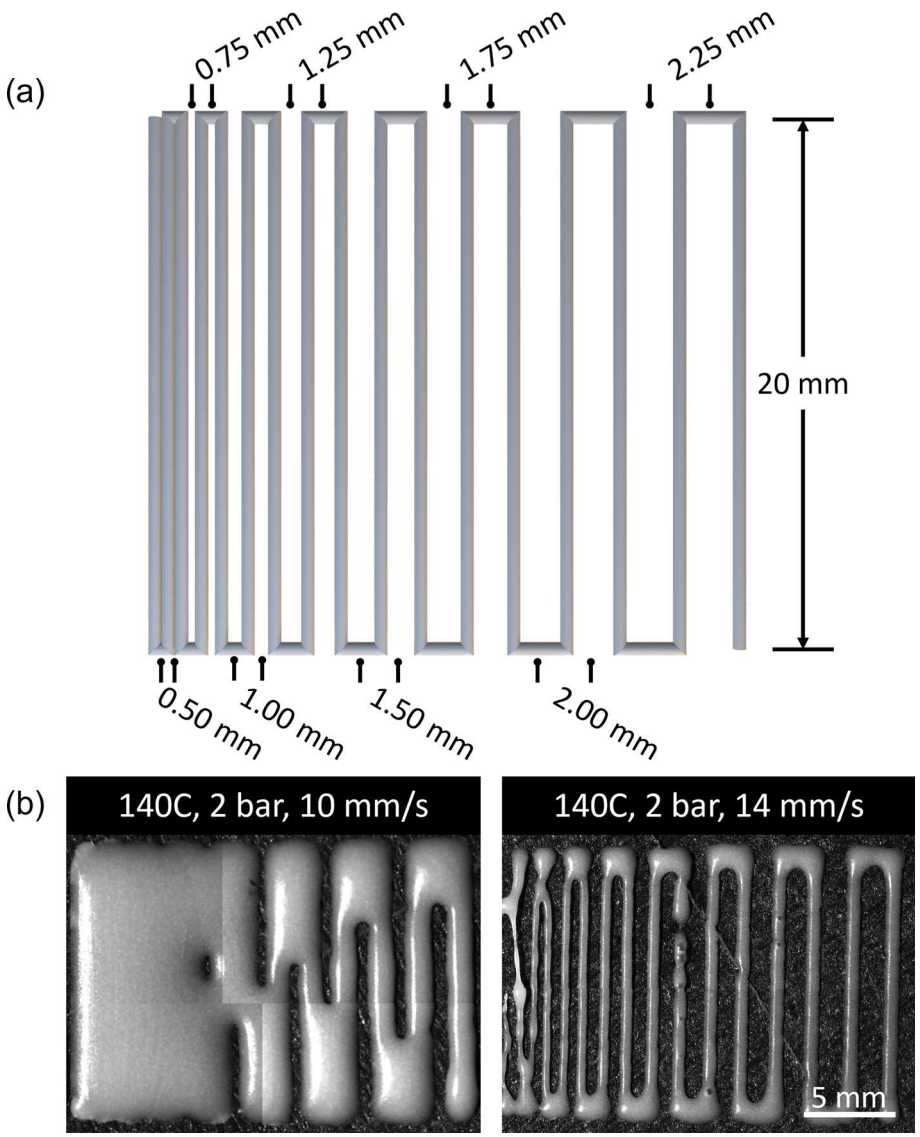

Fig. 6 Strand fusion analysis of print parameter combinations. **a** Theoretical fusion test with interstrand gaps ranging from 0.5 to 2.25 mm, with each interstrand gap printed twice per artifact. **b** Effect of print speed on strand fusion. Insufficient print speed for the developed flow yields significant fusion (left) than when print speed more closely matches the flow, yielding nominal fusion (right)

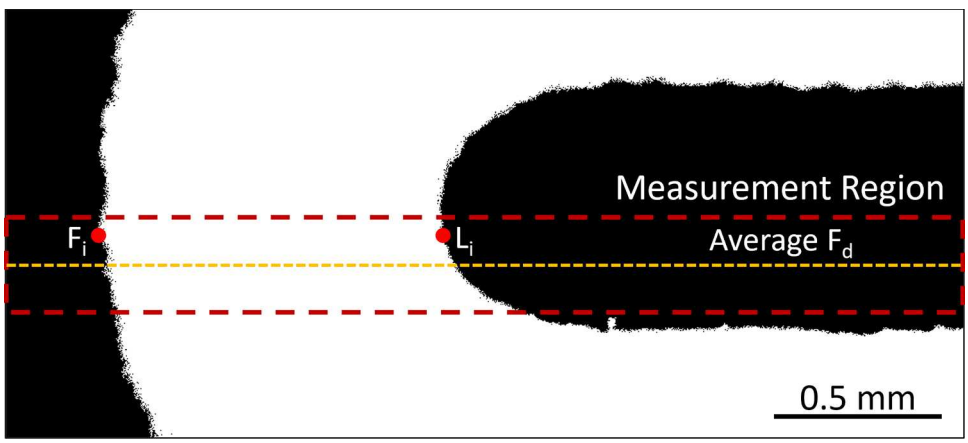

Fig. 7 Fusion length quantification process in a turnaround's measurement region through a pixel-wise, 100-point average of local fusion length

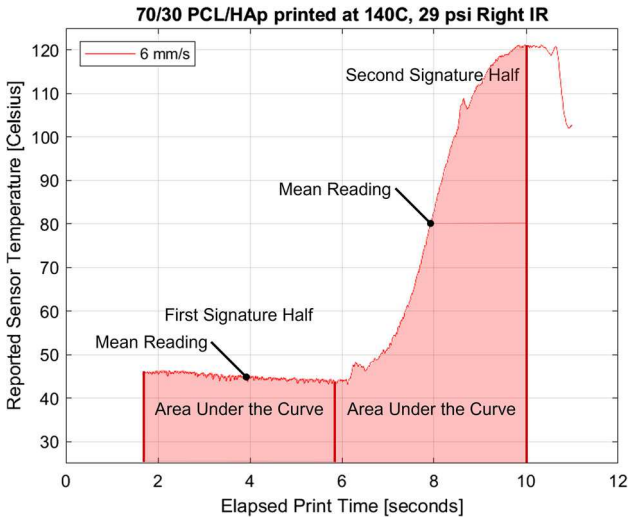

Fig. 8 Sensor feature extraction process from the raw in-situ sensor signals for single strand quality testing

Feature extraction from in-situ sensor data

In Sect. "Experimental design", each experimental phase was detailed regarding the target classes or metrics constructed from the experimental performance. In this section, feature extraction from in-situ IR thermocouples is elucidated. Machine learning used these features as inputs for quality classification and prediction. The in-situ IR thermocouples collected data at a 500 Hz sampling rate. However, the thermocouples were not calibrated to produce true temperature approximations for the print material, as the emissivity of the material is not compensated. As a result, only the relative trends in the sensing data are considered.

We note that the thermocouples are factory calibrated against a blackbody source. However, the difficulty in measuring exact temperature of the deposited material using non-contact, IR-based instruments due to changes in emissivity remains an open challenge not only in extrusion-based printing but the larger realm of additive manufacturing (Lane & Whitenton, 2016).

Single strand quality

Individual strand signatures were isolated from the raw signal, and the signature was divided into two halves. Using signal halves considers the difference in performance between the first half and second half of a strand into account by allocating the feature values from corresponding regions in the signal. Figure 8 illustrates the difference in the strand halves and the associated signals, where the first half's smaller strand width is coupled with a shorter signal profile. While quartering the signal was also conducted to assign corresponding features to each imaging location, this did not significantly change the results. As a result, dividing the signal into two halves for a strand was chosen as the feature extraction methodology.

Each sensor signature half was assessed to produce the average reading, standard deviation, and area under the curve (Fig. 8). As the infrared thermocouples receive radiated heat from the area they are focused on, the more high-temperature material in that area, the higher the reading (until the entire area is full of the high-temperature material). As shown in Fig. 8, the average reading indicates the degree of extrusion, with high temperature and pressure cases leading to high average readings and low temperature–pressure combinations leading to low average readings. In under-extrusion, strands can be variable in width or discontinuous, leading to an increased signal standard deviation.

The area under the curve was determined through trapezoidal integration, with a step size of 2 ms. The higher the signal profile (as with high-temperature, high-pressure printing), the larger the area under the curve. Because each print speed takes a different amount of time to complete the 50 mm strand, the area under the curve was divided by strand completion time to standardize to an average area. Six features were formed following the measurement phase, three features from each thermocouple (average reading, standard deviation, and area under the curve), and the values were assigned to the appropriate strand half.

Strand fusion assessment

Each artifact signature was isolated from the raw signal and divided into eight segments, with each segment corresponding to a specific interstrand gap. For a specific interstrand gap, this signature region contained the data starting from the center of a strand, progressed through the two turnarounds, then ended at the center of a strand. Under this method, only sections pertaining to the specific turnarounds and interstrand spaces were observed. The turnaround segments were then assessed to produce the average reading, standard deviation, and the area under the signal curve (Fig. 9). In this testing phase, distinct cycling was observed, where the peaks in the signature corresponding to the printing of the gap turnarounds. In each signal, 18 peaks were observed, where the first 16 were from the printing of the fusion sample, and the final two were the movements to the following sample location. As a result of the cycling, the signal region of a set interstrand gap and its replicate could be isolated (see Fig. 9) and assessed to produce the sensing features (average reading, standard deviation, and the area under the signal curve). The area under the curve was determined through trapezoidal integration, with a step size of 2 ms. Six features were formed following the measurement phase, three features from each thermocouple (average reading, standard deviation, and area

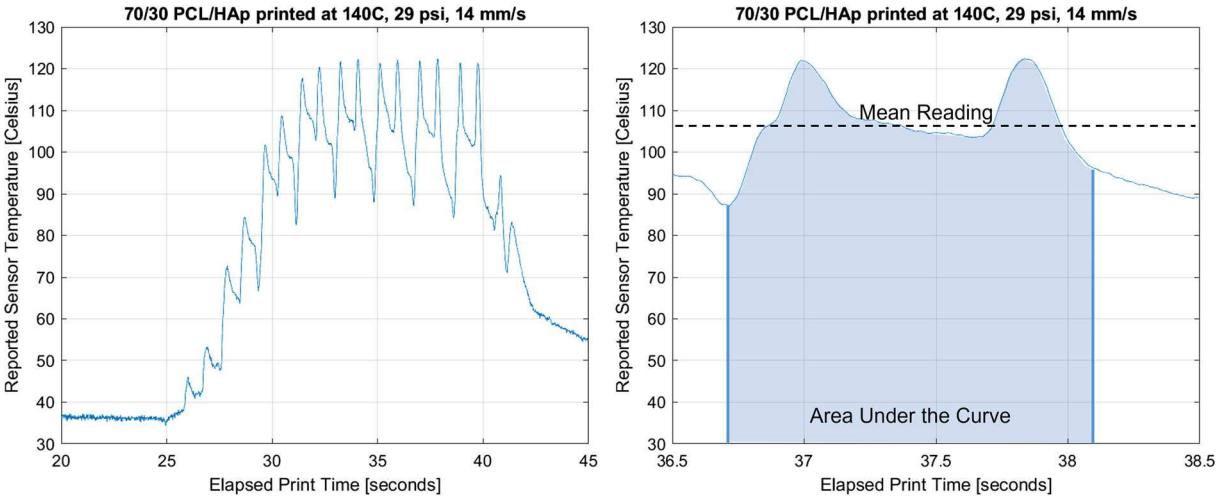

Fig. 9 Sensor feature extraction process from the raw in-situ sensor signals for strand fusion testing. (Left) Raw signal from a fusion test print. (Right) An isolated signal region of the two replicates of a set interstrand space is used for the feature extraction

under the curve), and the values were assigned to the appropriate interstrand gap.

Quality prediction using machine learning

Six supervised machine learning models were optimized and deployed to classify or predict performance for each experiment (single strand and strand fusion) based on in-situ IR thermocouple sensing features. Simple baseline models were run for comparison purposes to avoid overfitting.

The machine learning applications presented in this work are divided into four distinct tasks, as shown in Fig. 10. These tasks are as follows: Task 1—print regime classification, Task 2—strand width prediction, Task 3—strand height prediction, and Task 4—strand fusion severity prediction. The coupling of the extrusion flow and print speed is assessed in the first task, print regime classification. Specifically, the in-situ sensing features were used to classify a strand into the over-extruded (larger than desired), under-extruded (smaller than desired or demonstrating variable deposition), or ideal extrusion print regime.

In the second and third tasks, strand width and height prediction, respectively, the in-situ sensing features were used to predict the average width and height of the printed strand. Finally, in the fourth task, strand fusion prediction, the in-situ sensing features were used to determine the severity of strand fusion at the turnaround regions in a artifact. The severity of strand fusion was assessed as the ratio between the fused length and the design length of 0.6 mm.

In classification tasks, nonlinear multinomial statistical logistic regression served as the baseline model for comparison, while prediction tasks utilized Ridge regression for the baseline model. In addition to the baseline statistical model for a machine learning task, the following models were used; K-nearest neighbors (KNN), support vector machine (SVM), Random Forest, and shallow artificial neural network (ANN) with a maximum of three hidden layers. These models are selected owing to their ease of interpretability, popularity, and relative simplicity of online implementation through readily available modules in various programming languages. In addition, these models can accommodate relatively smaller data sets. Notably, the SVM, KNN, and RF models do not incorporate as active of a learning aspect as an ANN. A central hypothesis of this work is that physically interpretable features in simple machine learning models would provide sufficient flaw detection fidelity, as opposed to complex black-box approaches, such as deep learning.

Hyperparameter tuning was conducted with tenfold cross-validation to determine the optimal settings for each model, Table 1 describes the hyperparameters for each model. Training and testing of each machine learning model followed an 80–20 scheme, wherein 80% of the dataset was used for training, and the trained model was tested on the remaining 20% of the data. The total amount of data and the datapoint count allocated to training and testing is shown in Table 2.

In tenfold cross-validation, the training data is divided into ten approximately equal-sized parcels, then nine parcels are used for training, while the last is used for validation. Once the train-validate process is completed, a fold is complete, and the process repeats until each parcel has been held out for validation. Validation results were averaged over the ten folds, and the hyperparameter combinations which yielded the highest performance were chosen for the final machine learning models.

Model training was conducted on a laptop computer with the following specifications: AMD Ryzen 9 5900HX and 2 × 8 GB 3200 MHz DDR4 memory. All machine learning was conducted using Python software with the Scikit-learn

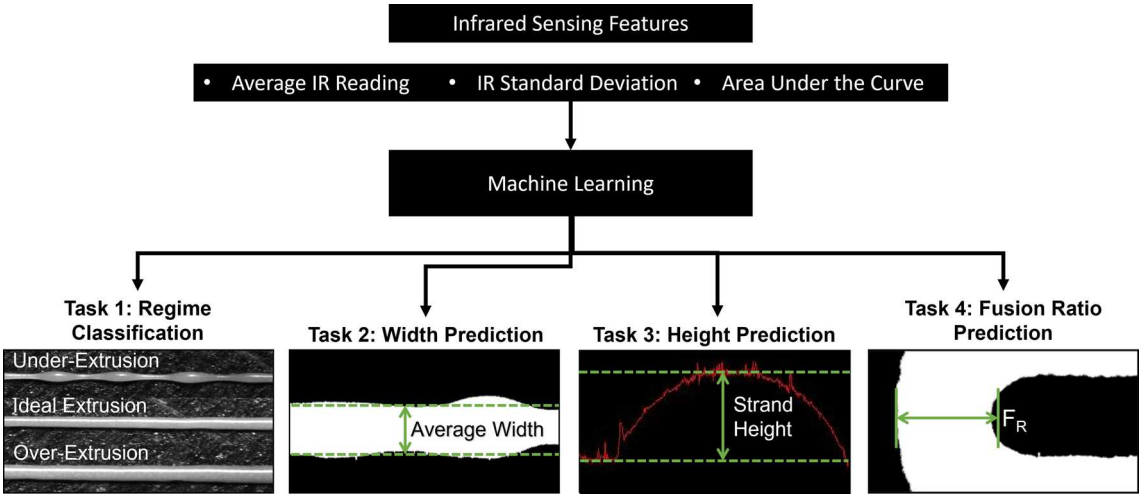

Fig. 10 Machine learning tasks for each testing phase: single strand quality and strand fusion assessment

Table 1 Hyperparameters per machine learning model optimized with tenfold cross-validation

Machine learning approach	Tuned hyperparameters
Nonlinear multinomial logistic regression	No tuning was conducted
Ridge regression	No tuning was conducted
K-nearest neighbors	Number of neighbors, Distance metric, Weighting
Support vector machine	Regularization, Kernel type
Random forest	Number of estimators, Maximum tree depth, Maximum samples
Artificial neural network	Activation function, Regularization term, Hidden layer sizes

package (Pedregosa et al., 2011). The performance of the classification machine learning models was the testing F1 score, false positive rate (FPR, Type I error), and false negative rate (FNR, Type II error). The regression machine learning models were assessed using the coefficient of determination (R^2) and the root mean squared error (RMSE).

Preemptive feedforward quality control

The machine learning setup described in Sect. "Quality prediction using machine learning" was also applied for preemptive process control. This section assessed process parameter combinations and the resulting print quality to create more uniform, high-quality print designs. In Sect. "Process parameter-based quality prediction", the machine learning application and quality criterion will be discussed, and the chosen parameter arrangements and experiments will be detailed in Sect. "Print quality assessment".

The key idea is to use the a priori trained machine learning model in a feedforward manner—the machine learning model recommends how much the print speed must be changed *during the process* to obtain a uniform strand. This analysis was done before printing is started. In other words, instead of printing a strand under fixed conditions, the process parameter (print speed) is changed dynamically to accommodate for strand width variation. Existing empirical models are static in nature, and are not capable of incorporating such dynamic process changes.

Process parameter-based quality prediction

Machine learning was applied to three tasks, as shown in Fig. 11; regime classification, width prediction, and

Table 2 Number of data points in each experimental task and the allocations for training and testing the machine learning models

		Total datapoints	Training datapoints	Testing datapoints
Task 1	Regime classification	360	288	72
Task 2	Width prediction	360	288	72
Task 3	Height prediction	360	288	72
Task 4	Fusion ratio prediction	270	216	54

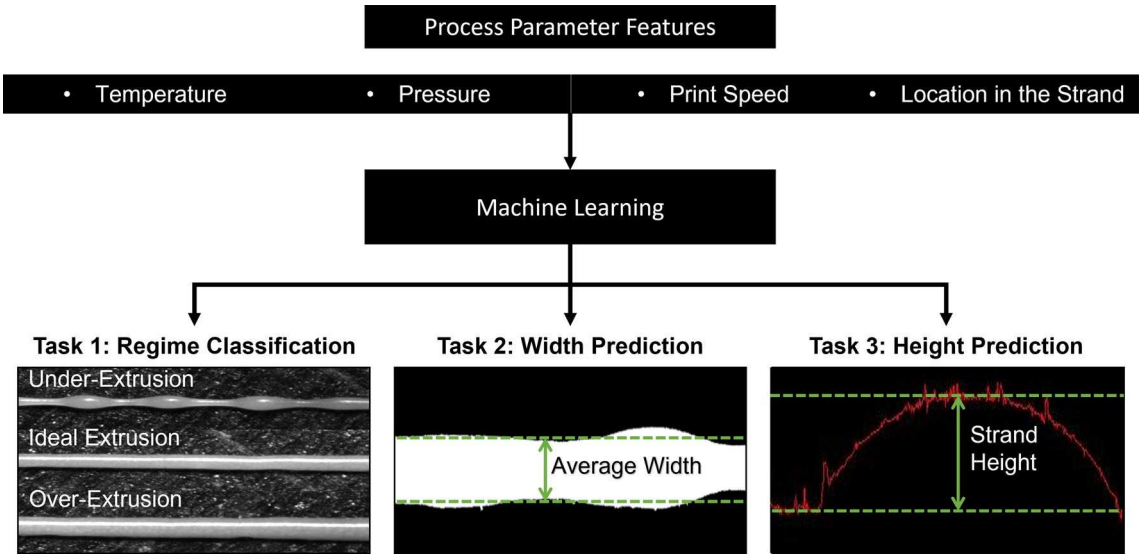

Fig. 11 Machine learning tasks for process parameter-based strand quality predictions

height prediction. As opposed to the features developed in Sect. "Feature extraction from in-situ sensor data", machine learning was conducted on the process parameters directly, namely, material temperature, extrusion pressure, print speed, and the location in the strand. Significantly, the location in the strand pertains to the imaging location along the print direction to determine strand homogeneity along its length.

Each location represents a 10 mm portion of the strand, and the first and last 5 mm of each 50 mm strand were omitted from imaging. As a result, location 1 refers to the section between 5 and 15 mm printed. At each location in the strand, the machine learning approach was used to classify the print regime and predict the strand width and height.

Machine learning performance was optimized as described in Sect. "Quality prediction using machine learning" with the hyperparameters and data allocations noted in Tables 1 and 2, respectively. Once trained and tested, the best-performing model was selected to provide quality predictions for preemptive quality control experiments. Print parameter arrangements were created by pairing an input print speed (the print speed for the first 25 mm of a strand) and an amended print speed (used after printing 25 mm). Input print speeds of 4, 5, 6, 7, 8, and 9 mm/s were fed into the machine learning systems with constant 130 °C and 2 bar, and strand quality metrics (regime, width, and height) were predicted for locations related to the first half of the strand. Next, a print speed sweep from 4 to 15 mm/s (with 1 mm/s step size) was conducted to predict the strand quality in the second strand half. The difference between the strand width of each half was calculated from the predictions. Print speed pairs were then constructed such that the strand widths of each strand half differed by less than 50 μm.

Table 3 Print speed arrangements producing comparable strand widths in each strand half

Printing at 130 °C and 2 bar			
Initial print speed (mm/s)	Initial width (mm)	Amended print speed (mm/s)	Amended width (mm)
4	0.59	11	0.6
5	0.58	11	0.6
6	0.53	13	0.5
7	0.53	13	0.5
8	0.53	13	0.5
9	0.46	15	0.5

Print quality assessment

Each initial print speed (4, 5, 6, 7, 8, and 9 mm/s) was paired with an amended print speed as discussed in Sect. "Process parameter-based quality prediction". Each pairing shown in Table 3 was then used to print six replicate 50 mm strands, imaged, and measured according to Sect. "Single strand quality". Notably, the first 25 mm of each strand was printed with the initial print speed before transitioning to the amended print speed for the remainder of the strand. In addition to the amended print speed experiments, constant print speed experiments were performed at print speeds of 4, 6, and 8 mm/s.

In addition to single strand testing, the parameter pairings in Table 3 were extended into fusion testing. As detailed in Sect. "Assessment of strand fusion" and Fig. 6, six replicates were printed for each interstrand space (0.5, 0.75, 1.00, 1.25, 1.50, 1.75, 2.00, and 2.25 mm). Further, fusion tests were

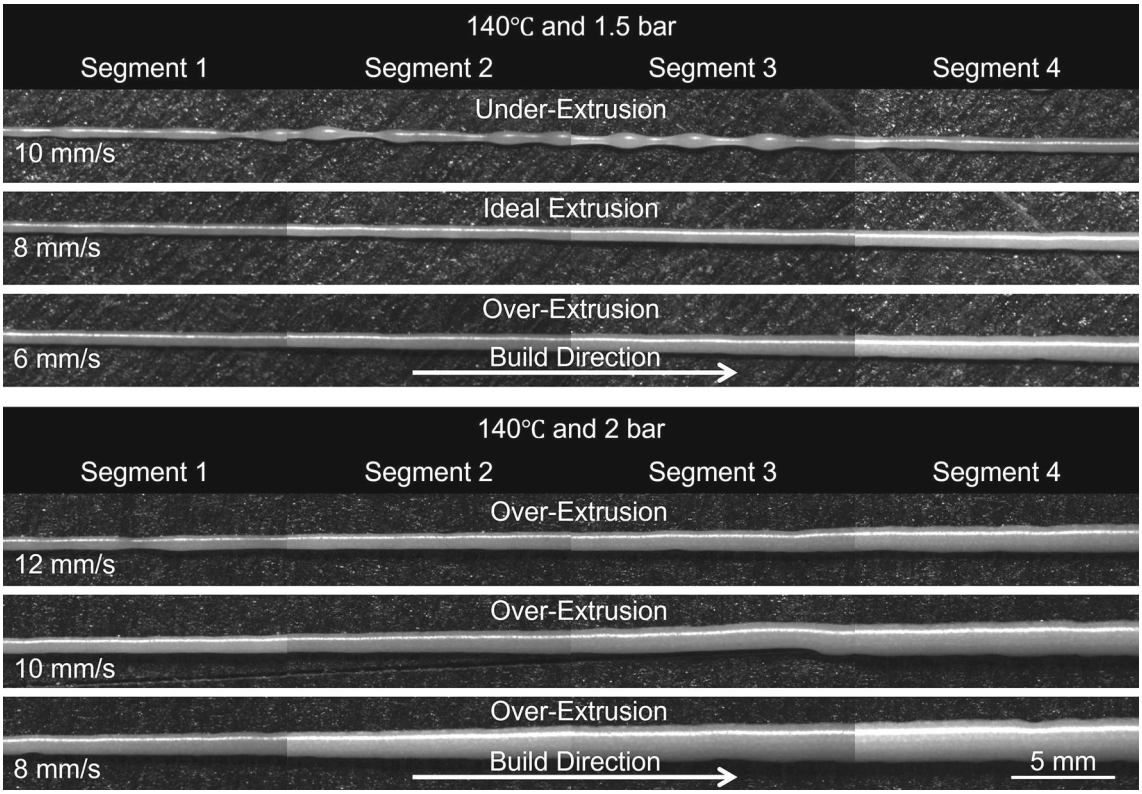

Fig. 12 Example strands at various print speeds and two pressure levels

printed for comparison at constant print speeds of 4, 6, and 8 mm/s.

Results

The following section details the application of machine learning models for the assessment of various print quality metrics. Model performance assessment metrics are discussed in Sect. "Quality prediction using machine learning". The presented machine learning models were trained with in-situ sensing features, as detailed in Sect. "Feature extraction from in-situ sensor data".

Single strand quality

Effects of process parameters on single strand quality

Strands are the fundamental unit upon which all artifact components depend. Therefore, strand quality prediction is imperative to address quality issues appropriately to avoid defective prints. For strand quality assessment, it is necessary to align with the desired strand width and height to avoid the accumulation of defects in subsequent layers. Notably, strand defects are correlated to the degree of localized deposition, and print speed adjustments result in localized deposition changes (see Fig. 12). When using excessive print speeds, localized deposition decreases significantly and can cause strand breakdown. Conversely, inadequate print speeds increase localized deposition, producing larger strands. Further, if the extrusion itself is changed, as with increased pressure (increasing extrusion), the compatible print speed window is shifted following a change in extrusion (see Fig. 12).

The trends evident in Fig. 12 are further supported by the experimental strand measurements presented in Fig. 13. In addition, Fig. 13 illustrates that both the width and height linearly increase along a strand. This trend is due to the flow reestablishing and material cooling in the print tip during the 25 s dwell time between strands. Due to the cooling effect, the material viscosity increases, and less material is extruded than the material at the desired print temperature. Once the cooler material is purged from the print tip, the strand steadily widens until reaching stable extrusion of the print material. Further, there is an inherent linkage between strand width and height. As the two qualities grow together, if either quality is undesirable, the remaining quality is likely undesirable. For example, an over-extruded strand not only would have a larger width than the design, but the strand height has the potential to supersede the design layer height, leading to defect accumulation in the subsequent layers.

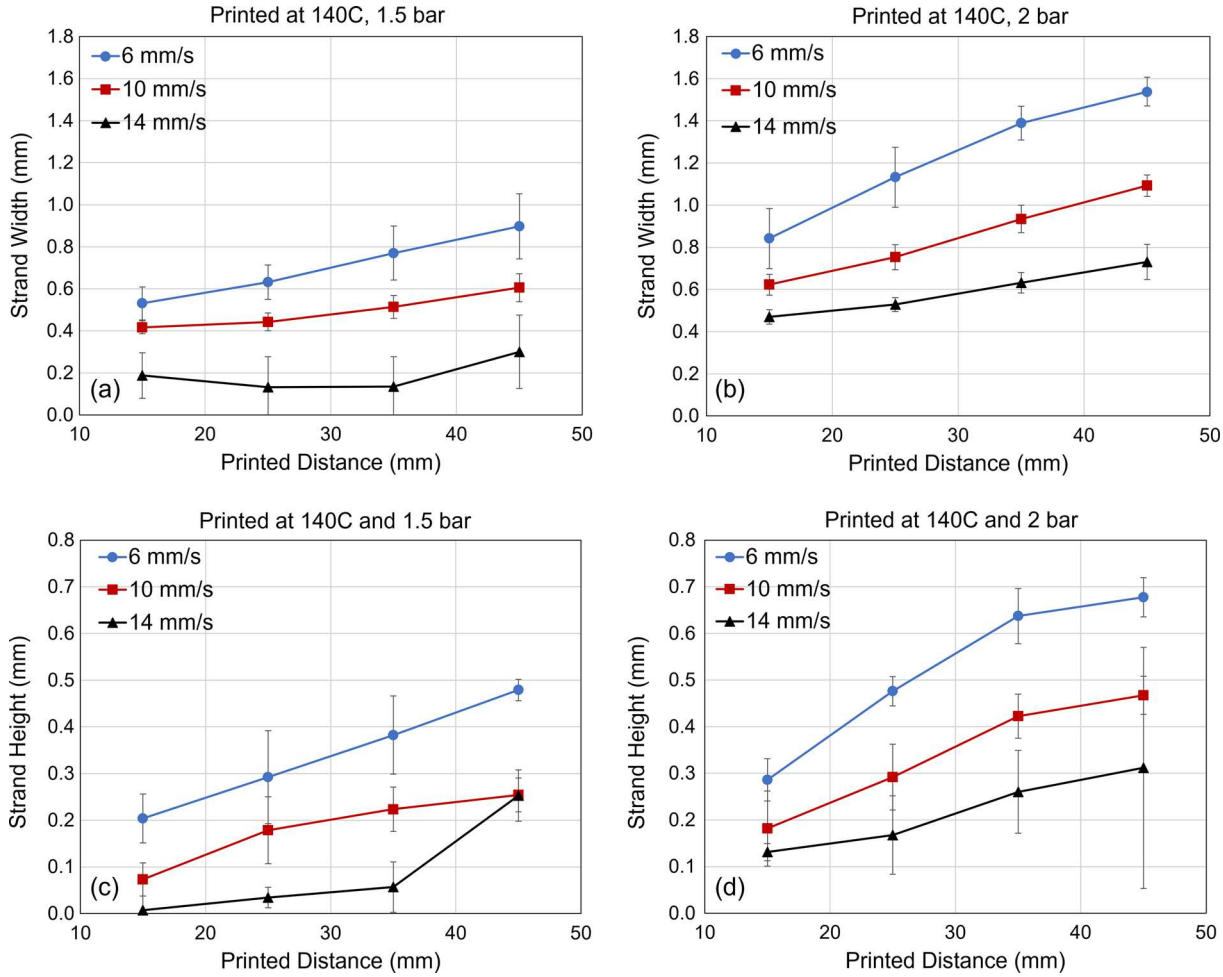

Fig. 13 Effect of pressure on strand width (**a**, **b**). At constant temperature and print speed, increasing pressure produces larger strand widths. Effect of pressure on strand height (bottom). Increasing pressure causes taller strands to develop at constant temperature and print speed

Once the strand measurements and the process parameter effects were visualized, the IR sensing features were analyzed for print regime classification. For comparison, example strands from the major print regimes were chosen, and their raw IR signals were plotted in Fig. 14. From Fig. 14, there are distinguished signal profiles, with over-extrusion yielding an elevated signal profile and under-extrusion yielding the smallest profile. Further, the under-extrusion case yielded beaded deposition as material delivery through the print tip was insufficient to consistently bridge the gap between the needle and substrate. During this under-extrusion, a droplet would form at the end of the print tip and grow until it touched the substrate. As a result of the droplet forming on the end of the print tip, the material was within the field of view of the thermocouple, but was cooling before deposition, potentially leading to the overall lower thermal profile in Fig. 14. Notably, each signal displays similar behavior early on, but the growth rate of the profile is inversely proportional to the print speed.

To avoid the complex analysis of the raw time-series data, strand signals were simplified into the average reading, standard deviation, and area under the curve for the first and second strand halves. As shown in Fig. 15, the signatures from a single thermocouple show a significant overlap in the features of the three print regimes. The overlap of features between print regimes in Fig. 15 makes it challenging to determine the print regime solely from the sensing features alone. This overlap is due to the difference in deposition between print speeds and the difference in strand width and height along the strand's length (see Fig. 13). Specifically, the first half of a strand had lower feature values (clustered in the bottom left of Fig. 15). The latter half had higher feature values (clustered in the top right of Fig. 15), making it difficult to split up the print regimes solely on the in-situ sensing feature values.

In addition, the correlations of the in-situ sensing features to the print regime are weak (Fig. 16). As a result, the subtle trends and differences in the sensing features must be

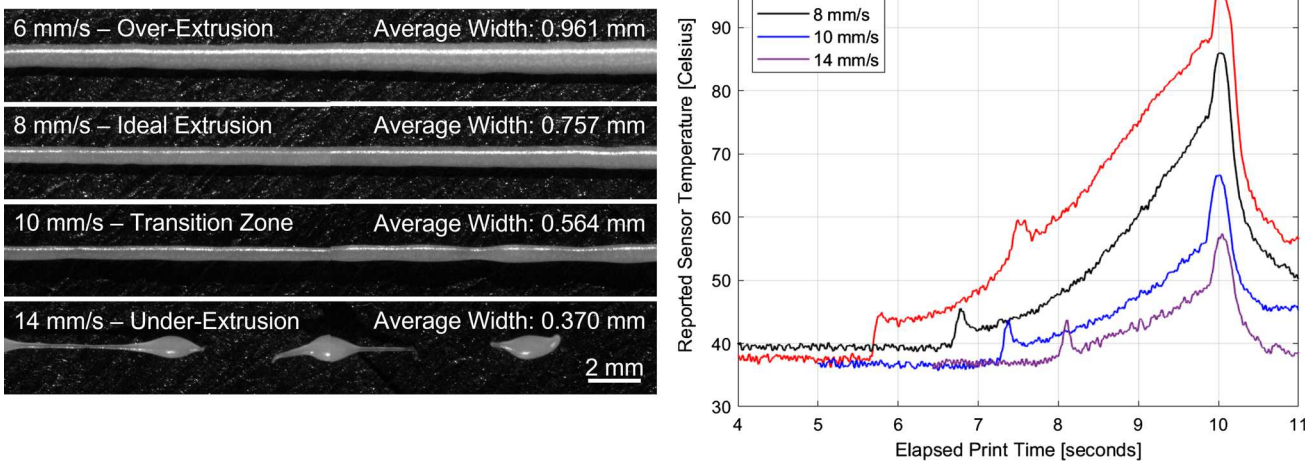

Fig. 14 Comparison of printed strands to the raw IR signal. (left) Strands demonstrating the four distinct behaviors: over-extrusion, ideal extrusion, under-extrusion, and the transition between ideal and under-extrusion. (right) The resulting raw IR signal from each strand shown to the left. As print speed increases, the strands become smaller, and there is a progressively diminished raw IR signal

captured through machine learning to distinguish between regimes. Further, prediction tasks to determine strand width and height are also dependent on encompassing the trends in the dataset with machine learning. While the correlations of the in-situ sensing features to the strand width and height targets (Fig. 16) are relatively larger than the print regime correlations, the machine learning results should benefit from the increased correlations. Notably, having high correlations implies that a feature and output have predictive capacity towards one another, which can aid the machine learning results.

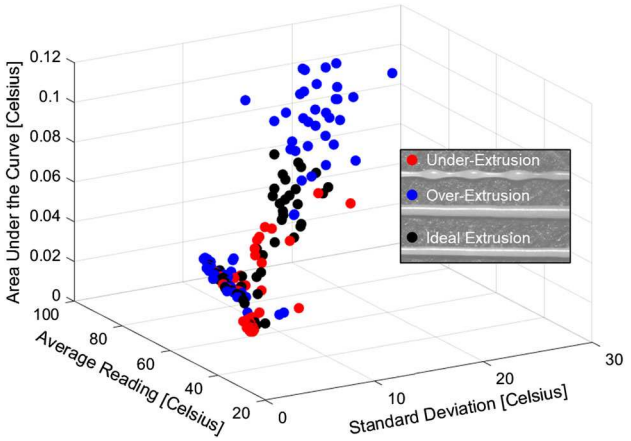

Fig. 15 3D plots of print regime versus the IR sensing features from one thermocouple. In-situ feature values and the associated print regime highlight the lack of clear boundaries in the print regime clusters

Single strand quality prediction results

Intuitively, strands can be either too small/discontinuous (under-extruded), ideally extruded, or excessively large (over-extruded). Assuming that stable extrusion is retained, strand height is proportional to the strand width, making regimes other than the ideal regime unfavorable for strand width and height. Therefore, if the print regime can aptly be classified in-situ, it allows for the determination of whether the print should be continued. Machine learning was applied to classify print regime from in-situ sensing features, resulting in high performance of both the baseline model (~ 86% F1 score) and the best performing machine learning models (~ 91%), as shown in Table 4. In addition to the high F1 scores for regime classification, all models display a higher FNR than FPR. In application, a lower FPR than FNR leads to fewer instances of incorrectly halted processes at the cost of potentially failing to detect an issue. Coupling the trends in the F1 scores and the FPR/FNR, misclassifications are rare and are unlikely to falsely determine that the quality requires the print to be halted.

While the print regime can provide an intuitive view of the printing process, the prediction of the strand width and height provide information about the severity of a divergence from the design specifications. For the prediction of strand width, favorable R^2 (~ 85%) was achieved for several models (KNN and Random Forest) along with low RMSE (~ 0.13 mm), as shown in Table 5. Similarly, the prediction of strand height produced R^2 (> 90%) with low RMSE (~ 0.13 mm) in the KNN model (see Table 5). In both tasks, the baseline model

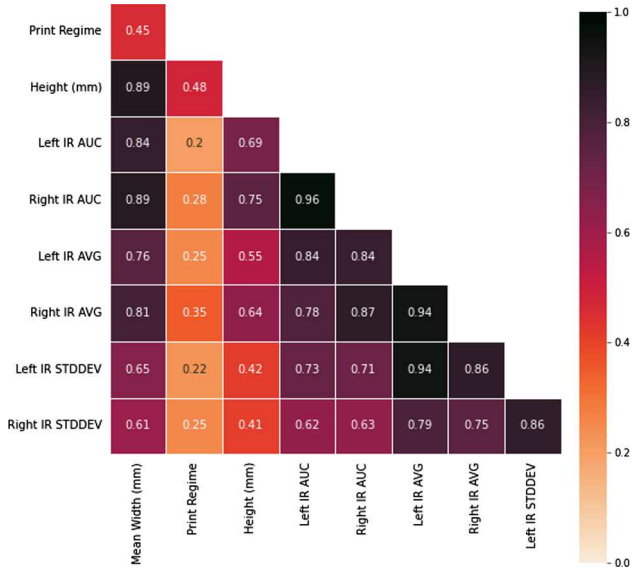

Fig. 16 Correlation matrix on the connection between print quality response variables (mean width, print regime, and strand height) and the IR sensing features (AUC area under the curve, AVG average reading, and STDDEV reading standard deviation). Higher correlations (values approaching 1 or − 1) indicate a relationship between two variables. AUC and AVG hold the highest correlations to print regime, mean width, and strand height, indicating that these features are more influential for the machine learning tasks

performed significantly worse than the other models, demonstrating the need for a different approach to the problem. Importantly, differences in the performance across machine learning models indicate how well the model assumptions fit the data.

While the input features for single-strand quality assessments are the same, the output targets are different (print regime, strand width, and strand height), making the distinction between the models a result of how well each model's assumptions fit the target data. Further, each machine learning model has limitations. For instance, Artificial Neural Networks generally need large datasets and more time to fit the data. However, the leading models perform nearly on par across the three tasks, demonstrating that a KNN or Random Forest could be applied to all tasks reliably. Given these results, the strand characteristics can be aptly predicted, as the best models can account for most of the variation in the dataset. Considering the regime, width, and height determination results, there is significant promise in incorporating in-situ sensing and machine learning into a process control strategy.

Table 4 Machine learning model performance for single strand quality classification. Each performance metric per column is the average from repeating the training and testing procedure 50 times, and one standard deviation is provided to contextualize F_1 Score performance

Machine learning approach	Task 1: regime classification	
	F1 score	FPR, FNR
Multinomial logistic regression	86.3 ± 0.0%	6.3%, 12.4%
K-nearest neighbors (KNN)	**91.8 ± 3.3%**	**4.1%, 8.1%**
Support vector machine (SVM)	76.6 ± 3.8%	11.6%, 23.1%
Random forest (RF)	90.7 ± 4.6%	4.6%, 9.2%
Artificial neural network (ANN)	79.7 ± 4.7%	10.1%, 19.9%

The bolded text highlights the best performing machine learning model for a task

Strand fusion assessment

Process parameter effects on strand fusion

The interaction between strands at turnaround regions is a pertinent indicator of the quality of a single layer. If the inter-strand gap or print speed is insufficient, strands interact at the turnarounds, propagating the fusion of the adjacent strands (see Fig. 17). In extreme cases, strand fusion can occur along

Table 5 Machine learning model performance for single strand quality prediction

Machine learning approach	Task 2: width prediction		Task 3: height prediction	
	R^2 value	RMSE	R^2 value	RMSE
Ridge regression	66.1 ± 6.5%	0.20 ± 0.02	54.0 ± 7.2%	0.10 ± 0.01
K-nearest neighbors (knn)	83.9 ± 2.8%	0.14 ± 0.01	**90.5 ± 4.1%**	**0.04 ± 0.01**
Support vector machine (SVM)	79.6 ± 3.8%	0.15 ± 0.01	69.3 ± 5.4%	0.08 ± 0.00
Random forest (RF)	**84.0 ± 4.8%**	**0.13 ± 0.01**	86.1 ± 5.9%	0.05 ± 0.01
Artificial neural network (ANN)	68.3 ± 7.6%	0.19 ± 0.02	55.2 ± 16.0%	0.10 ± 0.02

The bolded text highlights the best performing machine learning model for a task
Each performance metric per column is the average from repeating the training and testing procedure 50 times, and one standard deviation is provided to contextualize R^2 and RMSE performance

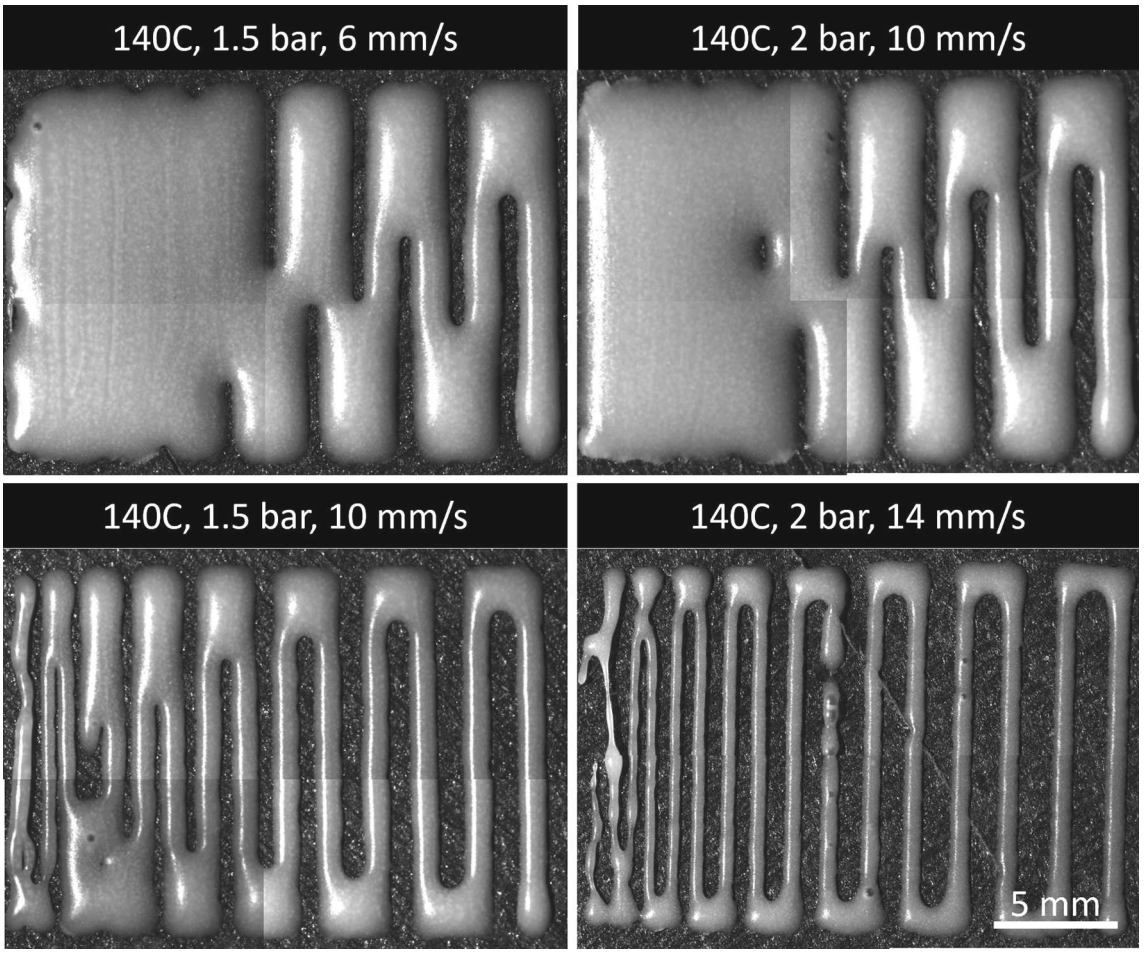

Fig. 17 Example fusion at various print speeds and two pressure levels

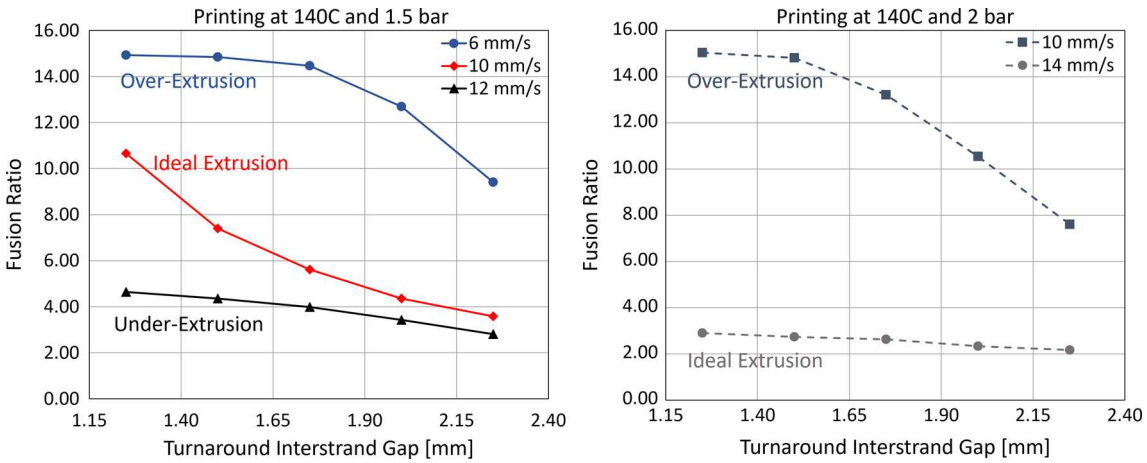

Fig. 18 Effect of print parameters on fusion ratio. Print speeds yielding over-extrusion led to severe fusion across all turnaround interstrand gap sizes. Increasing print speed resulted in the reduction of strand fusion

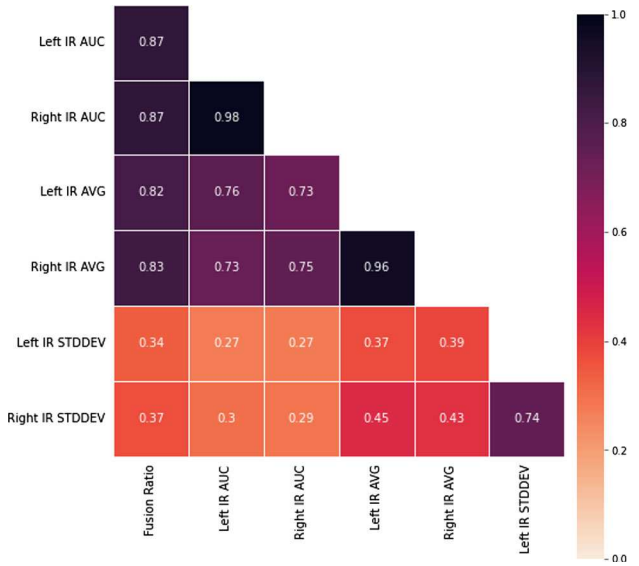

Fig. 19 Correlation matrix on the connection between print fusion ratio (column 1) and the IR sensing features (AUC area under the curve, AVG average reading, and STDDEV reading standard deviation). Higher correlations (values approaching 1 or − 1) indicate a relationship between two variables. AUC and AVG hold the highest correlations to print regime, mean width, and strand height, indicating that these features are more influential for the machine learning tasks

the entire strand length. Occasionally, the occlusion of intentional gaps for nutrient exchange can occur, diminishing the biological functionality of the artifact. As a result, strand fusion mitigation is vital to minimize the risk of fabricating an undesirable artifact. The experimental data (see Fig. 18) showed definite trends in the fusion ratio across pressures, print speeds, and resulting print regimes. As previously discussed, inadequate print speeds in the over-extrusion regime led to higher fusion ratios across the tested interstrand gaps. Further, print speeds yielding ideal and under-extrusion led to relatively lower fusion ratios. Therefore, increasing print speed can minimize the fusion ratio, but print speeds resulting in the under-extrusion regime should be avoided to prevent strand quality defects.

In the analysis of correlations between in-situ sensing features and strand fusion ratio (Fig. 19), strong correlations were seen in the AUC and mean reading features (> 0.8). Having high correlations implies that a feature and output have predictive capacity towards one another, which can aid the machine learning results. Because of these high correlations, it is vital to explore baseline models like Ridge regression using linear approaches to determine if moving to nonlinear approaches is truly necessary.

Strand fusion prediction results

Machine learning models were used to predict the fusion ratio at various interstrand gaps using features extracted from the IR thermocouple. The final machine learning results are shown in Table 6. During testing, severe fusion levels were present at the small interstrand gaps, so the interstrand gap range used for machine learning was limited to between 1.25 and 2.25 mm. Significantly, all the tested machine learning models tested similarly at an R^2 higher than 85%. In addition, each machine learning model demonstrated a reduction in the RMSE compared to the baseline Ridge Regression model. Given these results, strand fusion can be aptly predicted, as the best models can account for > 85% of the variation in the dataset.

Table 6 Machine learning model performance for strand fusion prediction

Machine learning approach	Fusion ratio prediction	
	R^2 value	RMSE
Ridge regression	82.5 ± 3.7%	2.02 ± 0.24
K-nearest neighbors (KNN)	86.0 ± 3.6%	1.80 ± 0.21
Support vector machine (SVM)	**88.6 ± 2.2%**	**1.75 ± 0.17**
Random forest (RF)	88.1 ± 2.3%	1.67 ± 0.20
Artificial neural network (ANN)	88.0 ± 2.9%	1.69 ± 0.23

Each performance metric per column is the average from repeating the training and testing procedure 50 times, and one standard deviation is provided to contextualize R^2 and RMSE performance

We note that in the case of strand fusion, the performance of the ridge regression classifier is comparable to other techniques, indicating the relative simplicity of strand fusion prediction compared to the previous three tasks. Due to this simplicity, models such as ANN that displayed poor performance in previous tasks due to the sparse nature of the data, perform at par with the preferred KNN and SVM models.

Preemptive process control

Strand quality control

In Sect. "Effects of process parameters on single strand quality", a strand widening effect was shown in Fig. 12 and quantified in Fig. 13, where strands grew broader and taller along the build direction. To overcome the drift in deposit characteristics, machine learning-based preemptive process control (feedforward control) was explored to correct the lack of strand homogeneity. The key idea was to alter the print speed by deploying machine learning on the dataset produced in the strand quality experiments described in Sect. "Single strand quality". In other words, the print speed change was determined before the strand was printed based on recommendations from the machine learning model. The print speed was selected as the control variable due to its short response time for adjustment compared to extrusion pressure,

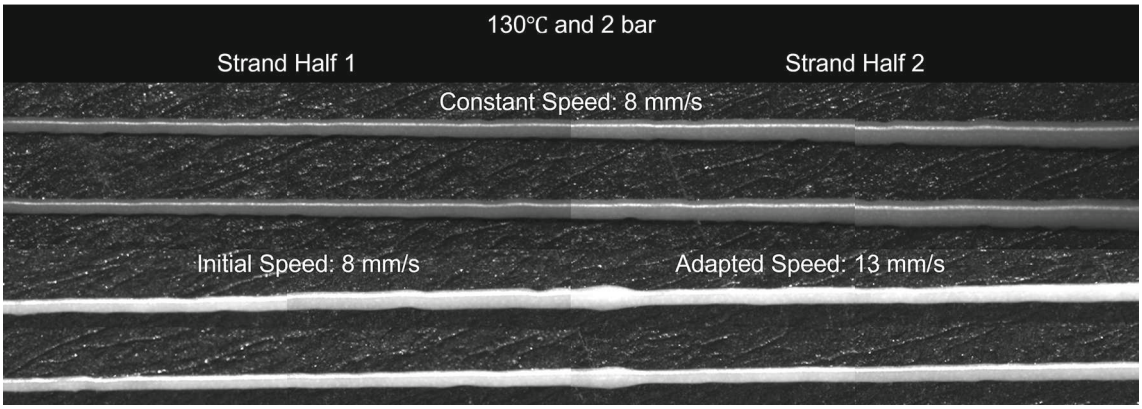

Fig. 20 Printing of strands at constant (top two rows) and amended print speeds (bottom two rows). In the top two rows, the strand is deposited at a constant speed of 8 mm/s. In amended speed samples, the initial print speed was changed to 13 mm/sec once 25 mm had been printed. This change in strand speed significantly mitigated the widening effect

which is adjusted pneumatically and is prone to activation delay-related errors due to an inherent lag.

Unlike the previous machine learning applications, only the process parameters were used to assess the process effects on strand quality at two locations in the strand, and in-situ sensor data was not used. In this phase, the machine learning models predicted the deposition regime, strand width, and height with statistical fidelity exceeding 90%.

An example of applying the print speed adjustments is shown in Fig. 20. In the top two rows of Fig. 20, single strands were printed at a constant 8 mm/sec speed. In the bottom two rows of Fig. 20, the strand speed was increased to 13 mm/sec after 25 mm of deposition based on insights from a trained machine learning model. This preemptive strategy of increasing the deposition speed significantly mitigated the widening effect. The transition region of print speed amended strands displayed a node due to the contrast between the widening initial strand half and the adjusted strand width following the transition. This sharp transition region is due to the abrupt change from the initial speed to the adapted speed and could be smoothed with a more gradual print speed change.

Continuing with this analysis, the approach was tested for various levels of constant print speed, namely, 4, 6, and 8 mm/s, i.e., the initial speeds in the print speed correction case. Homogeneity was assessed in the printed strands as the average width difference between the strand halves. As shown in Fig. 21, each constant print speed condition resulted in a statistically significant difference in the strand homogeneity. For example, when the print speed is maintained constant at 4 mm/s, the difference in width between the two strand halves exceeds 0.40 mm. The feedforward control strategy reduces the difference in strand width to less than 0.05 mm.

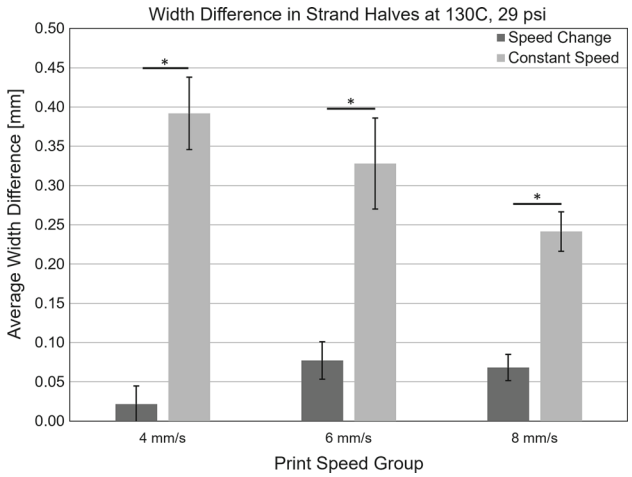

Fig. 21 Average strand width differences (± 1 standard deviation) between strand halves for strands printed with constant print speed and printed with a speed change to amend strand widening. Statistical analysis was conducted at a 95% confidence level, and significant differences are distinguished with an asterisk

Further, the consistency of the amendment quality was tested with the print speed amendments to the 4, 5, 6, 7, 8, and 9 mm/s initial speeds, as shown in Fig. 22. Print speed amendments were initially chosen to produce strand halves with a width difference of less than 50 μm. Figure 22 demonstrates the fulfillment of this < 50 μm width difference criterion at each initial print speed subject to the preemptive quality control scheme. Therefore, preemptive process control has the potential to improve strand quality significantly.

Strand fusion control

Following strand quality control testing, fusion testing samples underwent the same print speed amendments (Table 3).

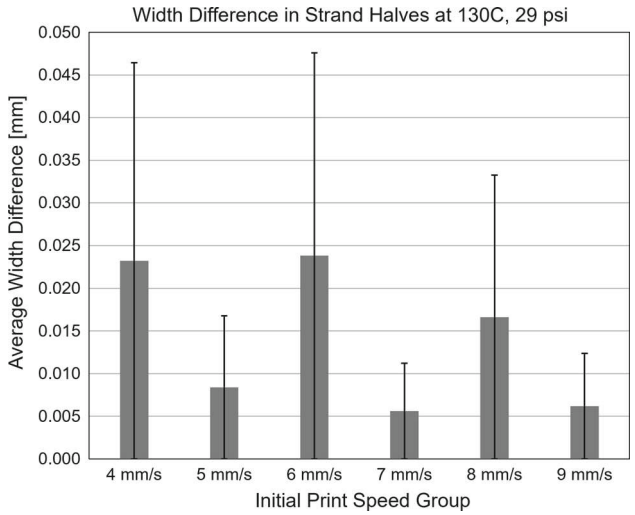

Fig. 22 Average strand width difference (± 1 standard deviation) across all initial print speed groups subject to print speed amendments

As previously discussed, strand fusion occurs if the interstrand gap or print speed is insufficient, causing strands to interact at the turnarounds, and propagating the fusion of the adjacent strands. Further, at constant temperature and pressure, localized deposition decreases if print speed increases, subsequently decreasing strand fusion in response. The constant print speed examples from Fig. 23 illustrate the effect of print speed on strand fusion, with the 8 mm/s interstrand gaps (Fig. 23c) demonstrating lower strand fusion ratios than the 4 mm/s case (Fig. 23a).

In the preemptive control experiments, a print speed amendment was administered after 25 mm were printed to maintain a more uniform strand width. Significantly, the amendments were not aimed at directly diminishing strand fusion but were purely to improve strand width homogeneity.

In the 4 mm/s trials shown in Fig. 23a, print speed was adjusted to maintain the width of the 4 mm/s strands, which had evident over-extrusion. As a result, the adapted print

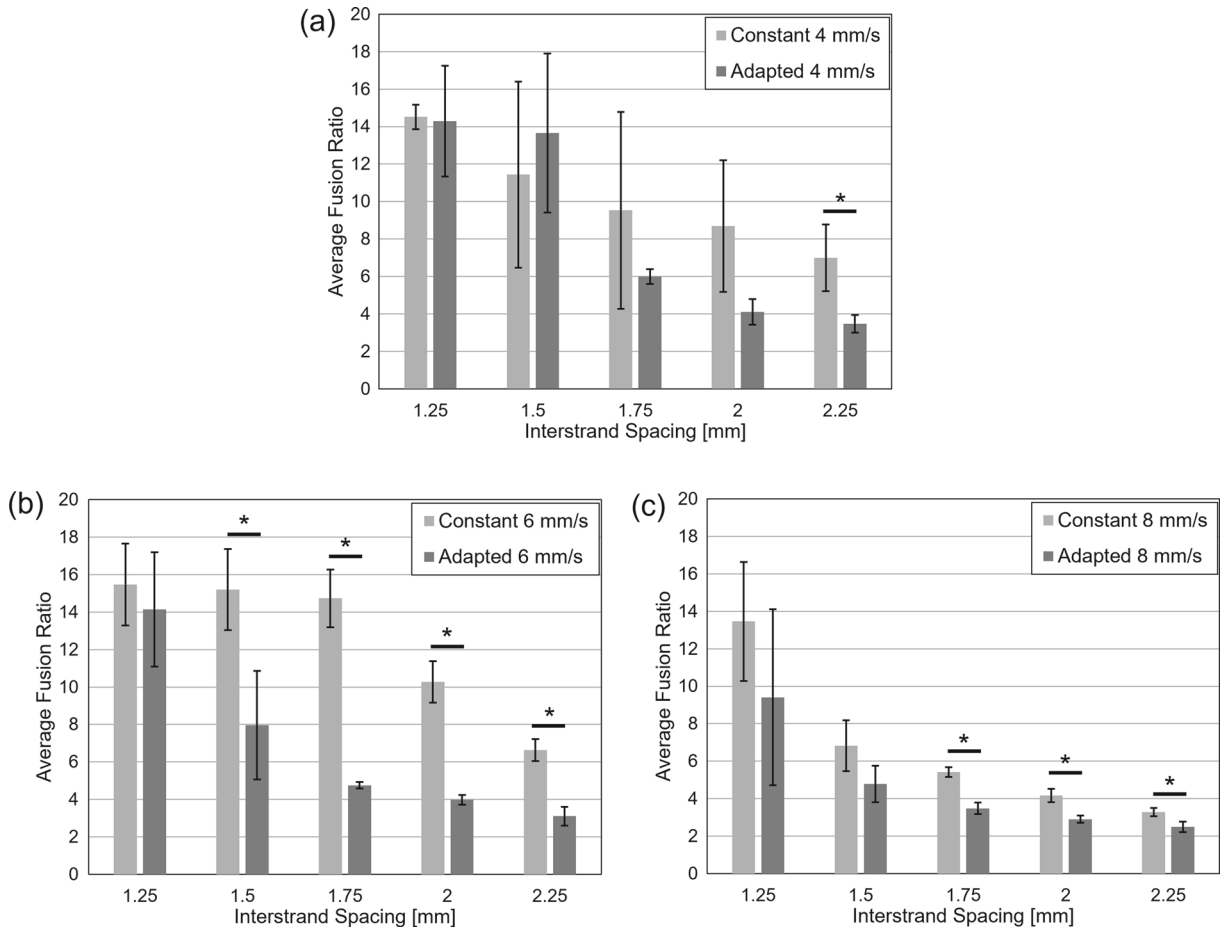

Fig. 23 Average fusion ratio measurement per interstrand spacing following printing with constant print speed versus adapted print speed. **a** Printing at a constant 4 mm/s and 4 mm/s adapted to 11 mm/s after 25 mm of printing. **b** Printing at a constant 6 mm/s and 6 mm/s adapted to 13 mm/s after 25 mm of printing. **c** Printing at a constant 8 mm/s and 8 mm/s adapted to 13 mm/s after 25 mm of printing. Results are shown as an average ± 1 standard deviation. Statistical analysis was conducted at a 95% confidence level, and significant differences are distinguished with an asterisk

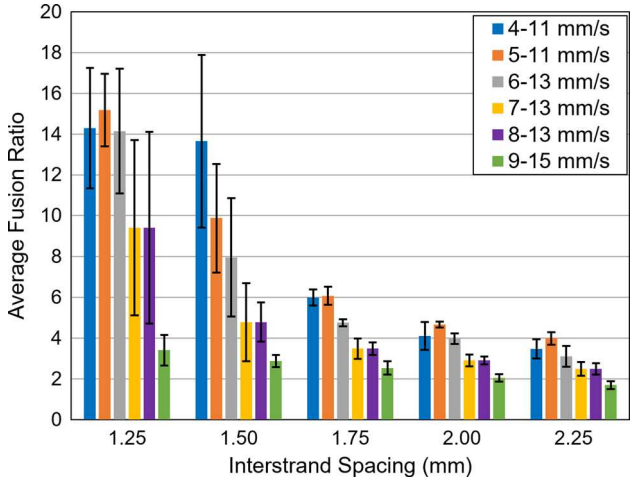

Fig. 24 Average fusion ratio measurement per inter-strand spacing following printing with an initial print speed followed by an adapted print speed after 25 mm were printed at 130 °C and 2 bar. Each test is shown in an initial print speed-adapted print speed format. For example, 4–11 mm/s indicates an initial print speed of 4 mm/s adapted to 11 mm/s after the transition point. Results are shown as an average ± 1 standard deviation

speed also featured over-extrusion, leading to large fusion ratios when printing small interstrand gaps. However, the adapted 4 mm/s print speed case yielded a statistically significant difference in fusion ratio at the largest interstrand gap of 2.25 mm.

The 6 mm/s trials (Fig. 23b) displayed ideal extrusion prior to the strand widening effect. Importantly, amending the print speed for a strand in the ideal extrusion regime yielded statistically significant decreases in the fusion ratio of interstrand gaps greater than 1.25 mm. Conversely, as the initial print speed was further increased to 8 mm/s (Fig. 23c), the strand width narrowed and became closer to the under-extrusion regime, reducing strand fusion both in the constant and amended print speed conditions. While the 8 mm/s speed yielded smaller strands and lesser strand fusion, the adapted print speed condition still reduced strand fusion in interstrand gaps measuring and surpassing 1.75 mm.

Additional testing was conducted to determine the reliability of the print speed amendment for strand fusion reduction. To improve the strand homogeneity, print speed amendments were made across the initial print speeds of 4, 5, 6, 7, 8, and 9 mm/s. The results of this testing are reported in Fig. 24, where the strand fusion ratio decreases with higher adapted print speeds. Further, the strand fusion ratios achieved at larger interstrand gaps ($\geq$ 1.75 mm) are more consistent, as evident by the lower standard deviations.

The results of both Figs. 23 and 24 signify that strand fusion can be reduced by controlling strand homogeneity. Further, this result remains true across a range of initial print speeds, including speeds that were not present in the initial training dataset (namely 4, 5, 7, and 9 mm/s). Therefore, this preemptive quality control method demonstrates a promising capability to improve part quality in both strand width at the 1D level and strand fusion at the 2D layer-level.

Conclusion and future work

This work investigated in-situ sensing and feedforward process control for quality assurance in extrusion-based biological additive manufacturing (Bio-AM). The relationships between printing process parameters, in-situ sensing features, and the resulting print quality were assessed. Critically, machine learning was deployed on the sensing features to determine four print quality indicators: print regime, strand width, strand height, and fusion ratio. By using solely in-situ sensing features, favorable performance (F_1 and R^2 scores $\geq$ 85%) was achieved from the best performing machine learning models.

Notably, the implemented defect detection machine learning models were agnostic to the input print parameters and were not reliant on an in-situ imaging system. This approach has two main advantages: (1) monitoring without process parameters is more focused on the developed extrusion degree, and (2) the lack of in-situ imaging removes the time-consuming imaging process between layers.

This project focused solely on one material composition and print tip diameter, but through additional testing, these models could be established for a wide range of print setups. Using machine learning, the required dataset for generalizing across a range of possibilities is smaller than the approach of purely applying process optimization approaches, as machine learning can approximate the performance of combinations in between known training data. In addition to sensing-based defect detection, a preliminary form of preemptive process control was displayed to correct the strand widening effect seen during testing.

Specific conclusions from this work were as follows:

- In-situ sensing was displayed with sufficient capacity for print quality monitoring during the printing process.
- Trained simple machine learning models for quality detection had F_1-score and R^2 approaching 85% in classification and regression problem performance.
- Machine learning was demonstrated as a feedforward process control of strand width homogeneity, leading to a statistically significant improvement in strand width homogeneity, to < 50 μm difference between the first and second half of a strand.

In closure, we acknowledge the need for additional biomedical studies to validate the effect of minor variation in strand width and resolution amounting to tens of microns on

functional properties, such as stiffness, media diffusion and cell proliferation in Bio-AM scaffolds. However, in addition to the biological functionality, it is imperative that printed scaffolds have sufficient geometric accuracy to avoid problems with a scaffold-transplant site dimensionality mismatch, or improper mechanical properties for the application. In our previous work, we provided insights into the effect of scaffold flaws on mechanical properties, but the relationship to biological functionality remains to be investigated (Sam Gerdes et al., 2020).

We also note the relative fledgling stage of process monitoring and control in Bio-AM relative to metal additive manufacturing, where process prognosis has matured to large-scale practical parts implemented in the aerospace and defense industries. This study takes the crucial first step towards scaling process monitoring and control in the Bio-AM arena through rudimentary test artifacts.

In our future work we will endeavor to assess the fidelity of the proposed sensing modalities with regard to complex 3D structures, as well as devising enhanced non-contact sensing modalities, such as active ultrasound and acoustic emission.

Acknowledgements Financial support from the National Science Foundation (NSF CMMI-1719388, CMMI-1739696, and CMMI-1752069), the University of Nebraska-Lincoln, and Nebraska Tobacco Settlement Biomedical Research Enhancement Funds are gratefully acknowledged. Specifically, the concept of in-situ sensing for process monitoring and assessing the effect of process conditions on quality of deposits in 3D (bio)printing of biomaterials was funded through CMMI-1739696 (Program Officer: Dr. Bruce Kramer). The foregoing grant provided funding for Dr. Samuel Gerdes' Ph.D. studies, and travel to academic conferences.

Declarations

Conflict of interest No competing financial interests exist in this research.

References

Armstrong, A. A., Alleyne, A. G., & Wagoner Johnson, A. J. (2020). 1D and 2D error assessment and correction for extrusion-based bioprinting using process sensing and control strategies. *Biofabrication, 12*(4), 45023. https://doi.org/10.1088/1758-5090/aba8ee

Armstrong, A. A., Norato, J., Alleyne, A. G., & Wagoner Johnson, A. J. (2019). Direct process feedback in extrusion-based 3D bioprinting. *Biofabrication, 12*(1), 15017. https://doi.org/10.1088/1758-5090/ab4d97

Armstrong, A. A., Pfeil, A., Alleyne, A. G., & Wagoner Johnson, A. J. (2021). Process monitoring and control strategies in extrusion-based bioprinting to fabricate spatially graded structures. *Bioprinting, 21*, e00126. https://doi.org/10.1016/j.bprint.2020.e00126

Chen, H., Han, Q., Wang, C., Liu, Y., Chen, B., & Wang, J. (2020). Porous scaffold design for additive manufacturing in orthopedics: a review. *Frontiers in Bioengineering and Biotechnology*. https://doi.org/10.3389/fbioe.2020.00609

Cheng, Z., Cui, M., Shi, Y., Qin, Y., & Zhao, X. (2017). Fabrication of cell-laden hydrogel fibers with controllable diameters. *Micromachines*. https://doi.org/10.3390/mi8050161

Derakhshanfar, S., Mbeleck, R., Xu, K., Zhang, X., Zhong, W., & Xing, M. (2018). 3D bioprinting for biomedical devices and tissue engineering: a review of recent trends and advances. *Bioactive Materials, 3*(2), 144–156. https://doi.org/10.1016/j.bioactmat.2017.11.008

Gaikwad, A., Giera, B., Guss, G. M., Forien, J. B., Matthews, M. J., & Rao, P. (2020). Heterogeneous sensing and scientific machine learning for quality assurance in laser powder bed fusion—a single-track study. *Additive Manufacturing, 36*, 101659. https://doi.org/10.1016/j.addma.2020.101659

Gerdes, S., Mostafavi, A., Ramesh, S., Memic, A., Rivero, I. V., Rao, P., & Tamayol, A. (2020). Process–structure–quality relationships of three-dimensional printed poly(caprolactone)-hydroxyapatite scaffolds. *Tissue Engineering Part A, 26*(5–6), 279–291. https://doi.org/10.1089/ten.tea.2019.0237

Gerdes, S., Ramesh, S., Mostafavi, A., Tamayol, A., Rivero, I. V., & Rao, P. (2021). Extrusion-based 3D (Bio)printed tissue engineering scaffolds: process–structure–quality relationships. *ACS Biomaterials Science & Engineering, 7*(10), 4694–4717. https://doi.org/10.1021/acsbiomaterials.1c00598

Habib, A., & Khoda, B. (2019). Development of clay based novel hybrid bio-ink for 3D bio-printing process. *Journal of Manufacturing Processes, 38*, 76–87. https://doi.org/10.1016/j.jmapro.2018.12.034

Habib, A., Sathish, V., Mallik, S., & Khoda, B. (2018). 3D printability of alginate-carboxymethyl cellulose hydrogel. *Materials, 11*, 454. https://doi.org/10.3390/ma11030454

Haglund, L., Ahangar, P., & Rosenzweig, D. H. (2019). Advancements in 3D printed scaffolds to mimic matrix complexities for musculoskeletal repair. *Current Opinion in Biomedical Engineering, 10*, 142–148. https://doi.org/10.1016/j.cobme.2019.06.002

He, Y., Yang, F., Zhao, H., Gao, Q., Xia, B., & Fu, J. (2016). Research on the printability of hydrogels in 3D bioprinting. *Scientific Reports, 6*(1), 29977. https://doi.org/10.1038/srep29977

Heinrich, M. A., Liu, W., Jimenez, A., Yang, J., Akpek, A., Liu, X., et al. (2019). 3D bioprinting: from benches to translational applications. *Small (weinheim an Der Bergstrasse, Germany), 15*(23), 1805510. https://doi.org/10.1002/smll.201805510

Hölzl, K., Lin, S., Tytgat, L., van Vlierberghe, S., Gu, L., & Ovsianikov, A. (2016). Bioink properties before, during and after 3D bioprinting. *Biofabrication, 8*(3), 32002. https://doi.org/10.1088/1758-5090/8/3/032002

Hulbert, S. F., Young, F. A., Mathews, R. S., Klawitter, J. J., Talbert, C. D., & Stelling, F. H. (1970). Potential of ceramic materials as permanently implantable skeletal prostheses. *Journal of Biomedical Materials Research, 4*(3), 433–456. https://doi.org/10.1002/jbm.820040309

Jenkins, T. L., & Little, D. (2019). Synthetic scaffolds for musculoskeletal tissue engineering: cellular responses to fiber parameters. *Npj Regenerative Medicine, 4*(1), 15. https://doi.org/10.1038/s41536-019-0076-5

Jin, Z., Zhang, Z., Shao, X., & Gu, G. X. (2021). Monitoring anomalies in 3D bioprinting with deep neural networks. *ACS Biomaterials Science & Engineering*. https://doi.org/10.1021/acsbiomaterials.0c01761

Klawitter, J. J., Bagwell, J. G., Weinstein, A. M., Sauer, B. W., & Pruitt, J. R. (1976). An evaluation of bone growth into porous high density polyethylene. *Journal of Biomedical Materials Research, 10*(2), 311–323. https://doi.org/10.1002/jbm.820100212

Kuboki, Y., Jin, Q., & Takita, H. (2001). Geometry of carriers controlling phenotypic expression in BMP-induced osteogenesis and chondrogenesis. *JBJS*. https://doi.org/10.2106/00004623-200100002-00005

Lane, B., & Whitenton, E. (2016). *Calibration and measurement procedures for a high magnification thermal camera*. National Institute of Standards and Technology.

Lee, S. J., Lee, I. W., Lee, Y. M., Lee, H. B., & Khang, G. (2004). Macroporous biodegradable natural/synthetic hybrid scaffolds as small intestine submucosa impregnated poly(D, L-lactide-co-glycolide) for tissue-engineered bone. *Journal of Biomaterials Science, Polymer Edition, 15*(8), 1003–1017. https://doi.org/10.1163/1568562041526487

Mostafavi, A., Abudula, T., Russell, C. S., Mostafavi, E., Williams, T. J., Salah, N., et al. (2021a). In situ printing of scaffolds for reconstruction of bone defects. *Acta Biomaterialia, 127*, 313–326. https://doi.org/10.1016/j.actbio.2021.03.009

Mostafavi, A., Samandari, M., Karvar, M., Ghovvati, M., Endo, Y., Sinha, I., et al. (2021b). Colloidal multiscale porous adhesive (bio)inks facilitate scaffold integration. *Applied Physics Reviews, 8*(4), 041415. https://doi.org/10.1063/5.0062823

Murphy, C. M., & O'Brien, F. J. (2010). Understanding the effect of mean pore size on cell activity in collagen-glycosaminoglycan scaffolds. *Cell Adhesion & Migration, 4*(3), 377–381. https://doi.org/10.4161/cam.4.3.11747

Nehrer, S., Breinan, H. A., Ramappa, A., Young, G., Shortkroff, S., Louie, L. K., et al. (1997). Matrix collagen type and pore size influence behaviour of seeded canine chondrocytes. *Biomaterials, 18*(11), 769–776. https://doi.org/10.1016/S0142-9612(97)00001-X

Pedregosa, F., Varoquaux, G., Gramfort, A., Michel, V., Thirion, B., Grisel, O., et al. (2011). Scikit-learn: machine learning in python. *Journal of Machine Learning Research, 12*(85), 2825–2830.

Ramesh, S., Harrysson, O. L. A., Rao, P. K., Tamayol, A., Cormier, D. R., Zhang, Y., & Rivero, I. V. (2021). Extrusion bioprinting: Recent progress, challenges, and future opportunities. *Bioprinting, 21*, e00116. https://doi.org/10.1016/j.bprint.2020.e00116

Rao, P. K., Liu, J., Roberson, D., Kong, Z., & Williams, C. (2015). Online real-time quality monitoring in additive manufacturing processes using heterogeneous sensors. *Journal of Manufacturing Science and Engineering*. https://doi.org/10.1115/1.4029823

Ribeiro, A., Blokzijl, M. M., Levato, R., Visser, C. W., Castilho, M., Hennink, W. E., et al. (2017). Assessing bioink shape fidelity to aid material development in 3D bioprinting. *Biofabrication, 10*(1), 14102. https://doi.org/10.1088/1758-5090/aa90e2

Roosa, S. M. M., Kemppainen, J. M., Moffitt, E. N., Krebsbach, P. H., & Hollister, S. J. (2010). The pore size of polycaprolactone scaffolds has limited influence on bone regeneration in an in vivo model. *Journal of Biomedical Materials Research Part A, 92A*(1), 359–368. https://doi.org/10.1002/jbm.a.32381

Roy, M., Yavari, R., Zhou, C., Wodo, O., & Rao, P. (2019). Prediction and experimental validation of part thermal history in the fused filament fabrication additive manufacturing process. *Journal of Manufacturing Science and Engineering*. https://doi.org/10.1115/1.4045056

Samandari, M., Quint, J., Rodríguez-delaRosa, A., Sinha, I., Pourquié, O., & Tamayol, A. (2021). Bioinks and bioprinting strategies for skeletal muscle tissue engineering. *Advanced Materials, 12*, 2105883. https://doi.org/10.1002/adma.202105883

Scime, L., & Beuth, J. (2019). Using machine learning to identify in-situ melt pool signatures indicative of flaw formation in a laser powder bed fusion additive manufacturing process. *Additive Manufacturing, 25*, 151–165. https://doi.org/10.1016/j.addma.2018.11.010

Soltan, N., Ning, L., Mohabatpour, F., Papagerakis, P., & Chen, X. (2019). Printability and cell viability in bioprinting alginate dialdehyde-gelatin scaffolds. *ACS Biomaterials Science & Engineering, 5*(6), 2976–2987. https://doi.org/10.1021/acsbiomaterials.9b00167

Thattaruparambil Raveendran, N., Vaquette, C., Meinert, C., Samuel Ipe, D., & Ivanovski, S. (2019). Optimization of 3D bioprinting of periodontal ligament cells. *Dental Materials, 35*(12), 1683–1694. https://doi.org/10.1016/j.dental.2019.08.114

Tsuruga, E., Takita, H., Itoh, H., Wakisaka, Y., & Kuboki, Y. (1997). Pore size of porous hydroxyapatite as the cell-substratum controls BMP-induced osteogenesis1. *The Journal of Biochemistry, 121*(2), 317–324. https://doi.org/10.1093/oxfordjournals.jbchem.a021589

Webb, B., & Doyle, B. J. (2017). Parameter optimization for 3D bioprinting of hydrogels. *Bioprinting, 8*, 8–12. https://doi.org/10.1016/j.bprint.2017.09.001

Williams, J. M., Adewunmi, A., Schek, R. M., Flanagan, C. L., Krebsbach, P. H., Feinberg, S. E., et al. (2005). Bone tissue engineering using polycaprolactone scaffolds fabricated via selective laser sintering. *Biomaterials, 26*(23), 4817–4827. https://doi.org/10.1016/j.biomaterials.2004.11.057

Yang, S., Wang, L., Chen, Q., & Xu, M. (2021). In situ process monitoring and automated multi-parameter evaluation using optical coherence tomography during extrusion-based bioprinting. *Additive Manufacturing, 47*, 102251. https://doi.org/10.1016/j.addma.2021.102251

Yu, C., & Jiang, J. (2020). A perspective on using machine learning in 3D bioprinting. *International Journal of Bioprinting, 6*(1), 253. https://doi.org/10.18063/ijb.v6i1.253

Zehnder, T., Sarker, B., Boccaccini, A. R., & Detsch, R. (2015). Evaluation of an alginate–gelatine crosslinked hydrogel for bioplotting. *Biofabrication, 7*(2), 025001. https://doi.org/10.1088/1758-5090/7/2/025001